PHYSICS OF FLUIDS

https://aip.scitation.org/journal/phf

Accepted May 26th 2022

Comparative heat transfer analysis of γ-$Al_2O_3 - C_2H_6O_2$ and γ-$Al_2O_3 - H_2O$ electroconductive nanofluids in a saturated porous square cavity with Joule dissipation and heat source/sink effects

Thirumalaisamy K,[1, a)] Sivaraj Ramachandran,[1] Sivaraj Ramachandran,[b)] Ramachandra Prasad V,[a)] Anwar Bég O,[c)] Ho-Hon Leung,[b)] Kamalov F,[d)] and Vajravelu K[e)]

Department of Mathematics, School of Advanced Sciences, Vellore Institute of Technology, Vellore 632014, India.

(*Electronic mail: sivaraj.kpm@gmail.com)

(Dated: 26 May 2022)

Inspired by the applications in electromagnetic nanomaterials processing in enclosures and hybrid fuel cell technologies, a mathematical model is presented to analyze the mixed convective flow of electrically conducting nanofluids (γ–$Al_2O_3 - H_2O$ and γ–$Al_2O_3 - C_2H_6O_2$) inside a square enclosure saturated with porous medium under an inclined magnetic field. The Tiwari-Das model, along with the viscosity, thermal conductivity, and effective Prandtl number correlations are considered in this study. The impacts of Joule heating, viscous dissipation, and internal heat absorption/generation are taken into consideration. Strongly nonlinear conservation equations which govern the heat transfer and momentum inside the cavity with associated initial and boundary conditions are rendered dimensionless with appropriate transformations. The Marker-And-Cell (MAC) technique is deployed to solve the non-dimensional initial-boundary value problem. Validations with previous study are included. A detailed parametric study is carried out to evaluate the influences of the emerging parameters on the transport phenomena. When 5% γ–Al_2O_3 nanoparticles are suspended into H_2O base-fluid, the average heat transfer rate of γ–$Al_2O_3 - H_2O$ nanoliquid is increased by $25 \cdot 63\%$ compared with the case where nanoparticles are absent. When 5% γ–Al_2O_3 nanoparticles are suspended into $C_2H_6O_2$ base-fluid, the average heat transfer rate of γ–$Al_2O_3 - C_2H_6O_2$ nanofluid is increased by $43 \cdot 20\%$ compared with the case where nanoparticles are absent. Further, when heat source is present, the average heat transfer rate of γ–$Al_2O_3 - C_2H_6O_2$ nanofluid is $194 \cdot 92\%$ higher than that in the case of γ–$Al_2O_3 - H_2O$ nanofluid.

Keywords: Magnetized nanofluids, square cavity, MAC computation, Joule heating, porous medium.

I. INTRODUCTION

In 1995, at the Argonne National Laboratory in the United States, Choi and Eastman[1] introduced nanofluids which constitute colloidal suspensions of base-fluids containing metallic / non metallic / carbon-based nanoparticles. Aluminum oxide (Al_2O_3), silver (Ag), zinc (Zn), copper (Cu), ferric oxide (Fe_3O_4), magnesium oxide (MgO), silicon dioxide (SiO_2), titanium dioxide (TiO_2), etc., are some examples of widely used nanoparticles, and engine oil (C_8H_{18}), water (H_2O), ethylene glycol ($C_2H_6O_2$), kerosene ($C_{12}H_{26} - C_{15}H_{32}$), vegetable oil, etc., are some popular base-fluids. These base-fluids have relatively low thermal conductivities compared to the material (solid) nanoparticle's thermal conductivity. Nanoparticles can be combined with base-fluids in different percentages (volume fraction) and as such nanofluids provide an efficient heat transfer medium. The nanofluids contain $1 - 100$ nanometer sized nanoparticles that are evenly and stably distributed. The inclusion of nanoparticles improves the thermal conductivity and thereby enhance the heat transfer. The nanoliquids are extensively utilized as preferred fluids in several engineering, industrial, and manufacturing applications including heat exchangers, electronic cooling systems, biomedical devices, surface coating, lubrication, environmental remediation and petroleum recovery[2–12].

Alumina is an excellent engineering material that is made from kaolin or bauxite in various phases known as alpha (α), beta (β), and gamma (γ). α–alumina is a white puffy powder that is known as nano–alumina. It has a lower specific surface area and bears high temperatures. It is inert and has almost no catalytic activity. It is the most stable form of alumina that is utilized as a ceramic material. Other transitional alumina phases such as β–alumina and γ–alumina are mostly used as catalysts. The unit cell of β–alumina has two alumina spinel blocks and it is hexagonal in shape, with a lamellar structure. γ–alumina has high temperature resistance, inert, high specific surface, excellent dispersion, high purity and it is a nano-alumina. γ-alumina is the most widely used nano-powder among the transitional alumina phases and it is utilized in catalysis applications owing to its high surface area and good porosity characteristics. Therefore, many researchers have considered the γ–alumina nano-powder for heat transfer analysis[13]. Moghaieb et al.[14] performed an ex-

[a)]Department of Mathematics, School of Advanced Sciences, Vellore Institute of Technology, Vellore 632014, India.
[b)]Department of Mathematical Sciences, United Arab Emirates University, Al Ain, United Arab Emirates.
[c)]Multi-Physical Engineering Sciences Group (MPESG), Aeronautical and Mechanical Engineering Department, School of Science, Engineering and Environment, University of Salford, Manchester M54WT, UK.
[d)]Faculty of Engineering, Canadian University Dubai, Dubai, United Arab Emirates.
[e)]Department of Mathematics, Department of Mechanical, Material and Aerospace Engineering, University of Central Florida, Orlando, FL32816, USA.

perimental analysis to study the turbulent convective energy transmission of γ–$Al_2O_3 - H_2O$ nanoliquid in engine cooling systems. Nowrouzi et al.[15] carried out an experimental investigation using MgO, TiO_2 and γ–Al_2O_3 nanoparticles in carbonated water for wettability alteration in carbonate oil reservoirs. They noticed that the contact angle was reduced very effectively after adding the nanoparticles into carbonated water. Radwan et al.[16] conducted an experimental analysis of turbulent convective engine cylinder's head cooling using γ–Al_2O_3 nanoparticles mixed with distilled water with volume fractions of 1% and observed that for all distinct nanoparticle sizes, the convective coefficient was improved. Ganesh et al.[17] numerically investigated the heat-generation effect on γ–$Al_2O_3 - H_2O$ nanoliquid flow inside an enclosure with multiple obstructions of various shapes. They noticed that the average and local heat transfer rates are increased for increasing the volume fraction of nanoparticle and superior energy transmission is observed in the triangular barriers inside the enclosure.

In mixed convection, both the buoyancy and shear forces play a substantial role. In general, the buoyancy force enhances the flow and heat transfer profiles inside a cavity and magnifies the energy transmission rates from the heated surface. The buoyancy-driven force is prominent in natural convection and extensive works have been reported with both non-Newtonian and Newtonian fluids in a variety of different geometries including square, rectangular, triangular, and trapezoidal cavities. The mixed convection is relatively a challenging phenomenon to investigate. Mixed convection finds applications in solar collectors, biomedical engineering, ventilation of buildings, aerospace appliances, thermal exchangers, etc.[18] Many applications arise in energy consumption and therefore studies on mixed convective flows are very important in power systems including fuel cells. For example, Abbasian et al.[19] numerically investigated the collective shear and buoyancy force effects on Cu–water nanofluid circulation within an enclosure with sinusoidally heated vertical walls. They observed that decreasing Richardson number produces higher heat transfer rates. Dadavi et al.[20] experimentally investigated the mixed convection flow inside a vented cubical cavity filled with large solid low-conductivity spheres. They noticed that when Richardson number is less than 10, the heat transfer rate and flow structure scaling are the same as pure forced convection. Ishak et al.[21] applied the finite element technique to explore the features of mixed convective Al_2O_3-water nanofluid flow within an enclosure of trapezoidal shape with solid cylinder, observing that an increment in the Reynolds number and Richardson number enhances the heat transfer rate. Humayoun et al.[22] numerically investigated the mixed convection flow inside a lid-driven cavity and disclosed that for smaller values of Richardson number, the forced convection dominates and the shear forces due to lid movement have a superior impact.

Convective flows in porous media feature prominently in several technological areas including high-performance insulation for buildings, combustion in porous substrates, chemical catalysis reactors, poro-elastic transport in cartilage, packed-bed energy storage system, geo-hydrology, hybrid fuel cells, percolating hydrocarbons, geothermal reservoirs, and transdermal drug delivery[23–25]. Javed et al.[26] numerically scrutinized the energy transmission and natural convective flow within copper-water nanofluid-filled porous trapezoidal cavities. They noticed that as the Darcy number is increased, the strength of streamlines circulations is intensified and the isotherms are significantly modified. Mythili et al.[27] used a Crank-Nicolson technique to analyze the Casson fluid flow over different geometries saturated with a non-Darcy porous medium, observing that velocity profiles decrease with an increment in Forchheimer number. Khan et al.[28] numerically scrutinized the impact of mixed convective flow inside a porous cavity of square shape, showing that heat transfer improves with higher Darcy number (larger medium permeability) for large values of Grashof number. Raju et al.[29] numerically investigated the Marangoni convective nanofluid flow in a porous medium by adopting the Runge-Kutta method and shooting technique, noting that increasing porosity parameter accelerates the flow.

Magnetohydrodynamics (MHD) comprises the interaction of electrically conducting fluids and applied magnetic fields. The transport characteristics of electrically conducting fluids can be non-intrusively manipulated by an external magnetic field. Magnetic nanofluids constitute an important subset of nanomaterials and enable electrically conducting nanofluids with magnetic nanoparticles to be controlled via Hartmann magnetic body force. Heat transfer and fluid flow behavior can therefore be modified in such fluids with either static or alternating magnetic fields. A substantial number of investigations on convective flows with magnetic field effect have been reported due to emerging applications in magnetic material processing, crystal growth processes, biomagnetic fluid dynamics, electromagnetic sensors, fuel cells and electromagnetic pumps[30]. Reddy and Panda[31] numerically analyzed the MHD natural convective flow and energy transmission in Al_2O_3-water nanoliquid within a porous wavy-shaped trapezoidal cavity with differentially heated sidewalls, observing a significant enhancement in heat transfer characteristics for amplifying the impact of magnetic field. Javaherdeh et al.[32] applied the finite difference technique to analyze the free convective MHD nanofluid flow of copper oxide-water inside a wavy cavity and noticed that velocity of the fluid diminishes for enhancing the values of the Hartmann number. Hajatzadeh et al.[33] numerically studied the convective energy transmission in alumina-water nanoliquid transport within a square cavity with an external magnetic field. They exhibited that the rate of heat transfer and fluid velocity are reduced with stronger magnetic field. They further detected that the Nusselt number and temperature profiles are elevated by increasing magnetic field inclination from 0 to 45 degrees. Mansour et al.[34] presented the finite volume method based numerical simulations to examine the nanofluid flow of copper-water inside a C-shaped cavity with an inclined magnetic field effect. They observed that amplifications in the Hartmann number (magnetic body force parameter) values diminish the flow of the nanoliquid. Revnic et al.[35] numerically scrutinized the inclined magnetic field effect on $Al_2O_3 - Cu - water$ hybrid nanoliquid convection flow within an enclosure, noting

that an increment in the magnetic force declines heat transfer. Farhany et al.[36] numerically investigated the $Al_2O_3 - water$ nanofluid natural convective flow within an enclosure with an inclined magnetic field. They observed that by increasing the Hartmann number values, the average Nusselt number is reduced owing to suppression of the thermal buoyancy force and convective energy transmission with stronger magnetic field.

Internal heat absorption/generation occurs in several thermal engineering processes. Mahmoudi et al.[37] applied the lattice Boltzmann method to investigate the energy transmission performance of $Al_2O_3 - water$ nanoliquid inside an open enclosure with absorption or generation of heat subject to non-uniform thermal boundary conditions. They inferred that the rate of heat transfer is increased for amplifying the heat generation. Benazir et al.[38] numerically investigated the Casson fluid flow over different geometries with a non-uniform heat sink/source using the finite difference technique. They noticed that the heat transfer is considerably modified by the surface dependent heat sink or source parameter. Rashad et al.[39] numerically investigated the influence of heat absorption or generation on copper-water nanoliquid flow within a trapezoidal cavity under an inclined magnetic field using a SIMPLE algorithm and inferred that the rate of heat transfer is augmented strongly with heat absorption whereas it is suppressed with heat generation. Rashad et al.[40] numerically scrutinized the MHD mixed convective nanofluid flow in a U-shaped lid-driven cavity with partial slip discrete heating by employing the finite volume procedure. They encountered that heat transfer decreases for all values of heat source/sink parameter while enhancing the volume fractions. Massoudi and Mohamed[41] exhibited the finite element computations for the natural convective flow and energy transmission performance of water-diamond nanoliquid around a spinning elliptic baffle inside a cavity with Lorentz force and uniform heat generation/absorption effects. They found that the temperature profiles are enhanced inside the cavity with greater uniform heat generation whereas they are reduced with heat absorption parameter. Shah et al.[42] numerically analyzed the mixed convective $CuO - water$ nanoliquid flow inside a curved corrugated cavity. They inferred that the Nusselt number diminishes and temperature profiles augment with enhancing the heat sink coefficient. Further, the isotherms contours magnitudes significantly increase with greater heat generation parameter.

Joule heating (also known as ohmic dissipation) is an important phenomenon in magnetohydrodynamics and involves the dissipation of energy in viscous flows due to externally applied magnetic field interacting with conducting liquids. Joule heating therefore improves the heat transfer by utilizing electric current movement, which increases electrical conductivity and reduces dynamic viscosity effects. Inclusion of Joule heating in mathematical models therefore provides a more realistic appraisal of MHD transport characteristics. Rahman et al.[43] applied the finite element technique to investigate the ohmic heating effect on mixed convective heat transfer in an enclosure with a semi-circular source at one wall, under transverse magnetic field effect. They found that energy transmission reduces for augmenting values of the ohmic heating parameter. Ghaffarpasand[44] computed the MHD natural convective flow of $Fe_3O_4 - water$ nanoliquid within a cavity under the conjugate impacts of Lorenz force and Joule heating. He exhibited that the rate of heat transfer decreases for magnifying either the Eckert (dissipation) number or Hartmann number. Mehmood et al.[45] numerically scrutinized the hydromagnetic mixed convective flow inside an alumina-water nanofluid-filled square enclosure containing a heated square blockage, with the impact of Joule heating. They noticed that magnifications in the magnetic field and Eckert number increase the mean heat transfer inside the enclosure. Zahan et al.[46] presented a numerical simulation to investigate the magnetohydrodynamic mixed convective flow inside a hybrid nanoliquid-filled triangular enclosure with ohmic heating. They noticed that the Joule heating parameter has a minor influence on the isotherms and streamlines contours. Taghikhani[47] discussed the magnetohydrodynamic convection within a copper-water nanoliquid-filled enclosure with Joule heating. He observed that stream function values are increased and the mean heat transfer rate is reduced with greater Eckert number and so the ohmic heating has an inhibitive consequence on the convection inside the enclosure.

Viscous dissipation is associated with internal friction in viscous flows and is a significant factor in heat transfer in porous media. Alhashash et al.[48] numerically investigated the viscous dissipation impact on free convective flow inside a square porous cavity by utilizing a thermal non-equilibrium model and demonstrated that the mean heat transfer rate of solids increases and the mean heat transfer rate of fluid decreases with an augmentation in the modified conductivity ratio for all values of viscous dissipation parameter. Ghalambaz et al.[49] numerically analyzed the viscous dissipation effect on free convective flow within a square porous enclosure filled with a nanofluid by adopting the Buongiorno two-component homogenous nanofluid model. They disclosed that the heat transfer rate at the cold and hot walls are dissimilar owing to the viscous dissipation impact. Magnifying the Eckert number enhances the Nusselt number at the cold wall whereas at the hot wall the trend is reversed. Pop and Sheremet[50] numerically studied the viscous dissipation effect on natural convection flow within a differentially heated enclosure filled with a Casson fluid, observing that increasing the Eckert number generates a reduction in the rate of heat transfer. Haritha et al.[51] numerically presented the heat transfer and free convective nanofluid flow inside an enclosure by considering the viscous dissipation effect. They noticed that the isotherm magnitudes increase as the Eckert number upsurges.

An in-depth literature survey confirms that no investigation has been presented in the literature to examine the effects of Joule heating, viscous dissipation, heat source or sink on the mixed convective γ-$Al_2O_3 - H_2O$ and γ-$Al_2O_3 - C_2H_6O_2$ nanofluid flow inside an enclosure of square shape with cold and hot slits containing an isotropic porous medium under an oblique magnetic field impact. This constitutes the novelty of the current investigation which is motivated by emerging applications in hybrid electromagnetic fuel cells and nano-magnetic materials processing systems. The Tiwari-Das nanofluid model is adopted for this investigation. The slits

maintain a hot temperature are located at the centers of the left and right walls of the cavity. The cavity's horizontal walls feature a cold slit at the middle section. The governing equations subject to the initial and boundary conditions are formulated in the Cartesian coordinate system and non-dimensionalized with suitable transformations. The initial-boundary value problem in dimensionless form is then solved with the efficient MAC method[28,52]. Validations with previous study are included. Numerical results for isotherms, streamlines, and local Nusselt number are presented graphically for various key emerging parameters. The simulations present deep insights into the transport phenomena in magnetic nanofluid filled enclosure of relevance to fuel cell energy and biomedical materials synthesis applications[53].

II. MATHEMATICAL FORMULATION

Figure 1 visualizes the two-dimensional geometry that is to be analyzed. The unsteady, laminar, incompressible, mixed convective flow of electrically conducting γ-$Al_2O_3-H_2O$ and γ-$Al_2O_3-C_2H_6O_2$ nanofluids inside a porous cavity with vertical and horizontal walls of length (L) under an oblique magnetic field, is considered. The middle portions of the right and left walls are sustained at a higher temperature whereas the center portions of the bottom and top walls are maintained at a lower temperature. The enclosure contains a homogenous, isotropic, and non-deformable porous medium. Thermo-physical properties of the nanoliquid are presumed based on the Tiwari-Das model. The influences of Joule heating, internal heat generation/absorption and viscous dissipation are taken into consideration.

In Cartesian coordinates, based on the above considerations, the mass, momentum and energy conservation equations are expressed as follows to consider the magnetic nanofluid, Joule heating, heat absorption/generation coefficient, viscous dissipation and inclined magnetic field effects:[32,37,43,49]

$$\frac{\partial u}{\partial x}+\frac{\partial v}{\partial y}=0 \tag{1}$$

$$\frac{\partial u}{\partial t^*}+u\frac{\partial u}{\partial x}+v\frac{\partial u}{\partial y}=-\frac{1}{\rho_{nf}}\frac{\partial p}{\partial x}+\nu_{nf}\left[\frac{\partial^2 u}{\partial x^2}+\frac{\partial^2 u}{\partial y^2}\right]+\frac{\sigma_{nf}B_0^2}{\rho_{nf}}\left(v\sin\Theta\cos\Theta-u\sin^2\Theta\right)-\frac{\nu_{nf}}{K}u \tag{2}$$

$$\frac{\partial v}{\partial t^*}+u\frac{\partial v}{\partial x}+v\frac{\partial v}{\partial y}=-\frac{1}{\rho_{nf}}\frac{\partial p}{\partial y}+\nu_{nf}\left[\frac{\partial^2 v}{\partial x^2}+\frac{\partial^2 v}{\partial y^2}\right]-\frac{\nu_{nf}}{K}v+\frac{(\rho\beta)_{nf}}{\rho_{nf}}g(T-T_c)+\frac{\sigma_{nf}B_0^2}{\rho_{nf}}\left(u\sin\Theta\cos\Theta-v\cos^2\Theta\right) \tag{3}$$

$$\frac{\partial T}{\partial t^*}+u\frac{\partial T}{\partial x}+v\frac{\partial T}{\partial y}=\frac{k_{nf}}{(\rho C_p)_{nf}}\left[\frac{\partial^2 T}{\partial x^2}+\frac{\partial^2 T}{\partial y^2}\right]+\frac{Q_0}{(\rho C_p)_{nf}}(T-T_c)+\frac{\mu_{nf}}{(\rho C_p)_{nf}K}\left(u^2+v^2\right)+\frac{\sigma_{nf}B_0^2v^2}{(\rho C_p)_{nf}}+\frac{\mu_{nf}}{(\rho C_p)_{nf}}\left(2\left(\frac{\partial u}{\partial x}\right)^2+2\left(\frac{\partial v}{\partial y}\right)^2+\left(\frac{\partial v}{\partial x}+\frac{\partial u}{\partial y}\right)^2\right) \tag{4}$$

The initial and boundary conditions of the problem are specified in Table I. The thermophysical properties of base-fluids $(C_2H_6O_2\ and\ H_2O)$ and nanoparticle (Al_2O_3) are displayed in Table II.

The thermophysical properties of nanofluids are essential for improving the heat transfer characteristics of the working fluid. The physical and thermal properties of nanofluids are considered based on the Tiwari-Das nanoscale model and are presented as follows:

Density of the nanofluid:

$$\rho_{nf}=(1-\Phi)\rho_f+\Phi\rho_p \tag{5}$$

Nanofluid's heat capacitance:

$$(\rho C_p)_{nf}=(1-\Phi)(\rho C_p)_f+\Phi(\rho C_p)_p \tag{6}$$

Nanofluid's thermal expansion coefficient:

$$(\rho\beta)_{nf}=(1-\Phi)(\rho\beta)_f+\Phi(\rho\beta)_p \tag{7}$$

Nanofluid's thermal diffusivity:

$$\alpha_{nf}=\frac{k_{nf}}{(\rho C_p)_{nf}} \tag{8}$$

Nanofluid's electrical conductivity:

$$\frac{\sigma_{nf}}{\sigma_f}=\left[1+\frac{3(\xi-1)\Phi}{(\xi+2)-(\xi-1)\Phi}\right]\ \text{where}\ \xi=\frac{\sigma_p}{\sigma_f} \tag{9}$$

Thermal conductivity, dynamic viscosity and effective Prandtl number of the nanofluids are defined mathematically as follows[56,57]:

$$\frac{k_{nf}}{k_f}=4\cdot97\Phi^2+2\cdot72\Phi+1\ \text{for}\ \gamma-Al_2O_3-H_2O \tag{10}$$

$$\frac{k_{nf}}{k_f}=28\cdot905\Phi^2+2\cdot8273\Phi+1\ \text{for}\ \gamma-Al_2O_3-C_2H_6O_2 \tag{11}$$

$$\frac{\mu_{nf}}{\mu_f}=123\Phi^2+7\cdot3\Phi+1\ \text{for}\ \gamma-Al_2O_3-H_2O \tag{12}$$

$$\frac{\mu_{nf}}{\mu_f}=306\Phi^2-0\cdot19\Phi+1\ \text{for}\ \gamma-Al_2O_3-C_2H_6O_2 \tag{13}$$

$$\frac{Pr_{nf}}{Pr_f}=82\cdot1\Phi^2+3\cdot9\Phi+1\ \text{for}\ \gamma-Al_2O_3-H_2O \tag{14}$$

$$\frac{Pr_{nf}}{Pr_f}=254\cdot3\Phi^2+3\Phi+1\ \text{for}\ \gamma-Al_2O_3-C_2H_6O_2 \tag{15}$$

To reduce the equations (1) – (4) into non-dimensional form, the following non-dimensional quantities are considered:

$$U=\frac{u}{U_0};V=\frac{v}{U_0};X=\frac{x}{L};Y=\frac{y}{L};P=\frac{p}{\rho_f U_0^2};\theta=\frac{T-T_c}{T_h-T_c};t=\frac{t^*U_0}{L} \tag{16}$$

In dimensionless form, the governing equations by virtue of Eqn. (16) emerge as follows:

$$\frac{\partial U}{\partial X}+\frac{\partial V}{\partial Y}=0 \tag{17}$$

$$\frac{\partial U}{\partial t}+U\frac{\partial U}{\partial X}+V\frac{\partial U}{\partial Y}=-\left(\frac{\rho_f}{\rho_{nf}}\right)\frac{\partial P}{\partial X}+\left(\frac{\nu_{nf}}{\nu_f}\right)\frac{1}{Re}\left[\frac{\partial^2 U}{\partial X^2}+\frac{\partial^2 U}{\partial Y^2}\right]+\left(\frac{\sigma_{nf}}{\sigma_f}\right)\left(\frac{\rho_f}{\rho_{nf}}\right)\frac{Ha^2}{Re}\left(V\sin\Theta\cos\Theta-U\sin^2\Theta\right)-\left(\frac{\nu_{nf}}{\nu_f}\right)\frac{1}{Re\,Da}U \tag{18}$$

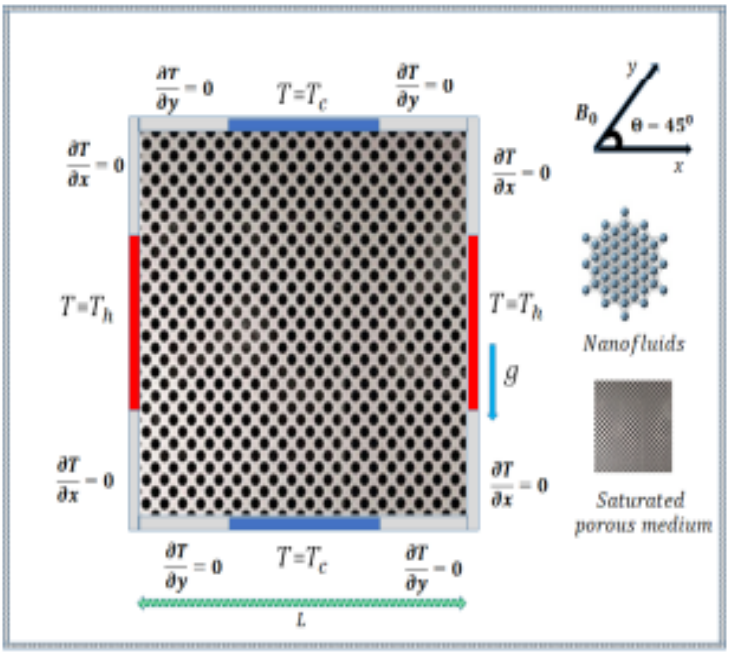

FIG. 1. Flow configuration of the problem

TABLE I. The initial and boundary conditions of the problem

Initial condition $t^* \leq 0$, $0 \leq x \leq L$, $0 \leq y \leq L$:	$u = v = 0$	$T = T_c$
Left wall $t^* > 0$, $x = 0$, $0 < y < L$:	$u = v = 0$	$\frac{\partial T}{\partial x} = 0$ for $0 < y < \frac{L}{4}$ $T = T_h$ for $\frac{L}{4} < y < \frac{3L}{4}$ $\frac{\partial T}{\partial x} = 0$ for $\frac{3L}{4} < y < L$
Right wall $t^* > 0$, $x = L$, $0 < y < L$:	$u = v = 0$	$\frac{\partial T}{\partial x} = 0$ for $0 < y < \frac{L}{4}$ $T = T_h$ for $\frac{L}{4} < y < \frac{3L}{4}$ $\frac{\partial T}{\partial x} = 0$ for $\frac{3L}{4} < y < L$
Bottom wall $t^* > 0$, $y = 0$, $0 < x < L$:	$u = v = 0$	$\frac{\partial T}{\partial y} = 0$ for $0 < x < \frac{L}{4}$ $T = T_c$ for $\frac{L}{4} < x < \frac{3L}{4}$ $\frac{\partial T}{\partial y} = 0$ for $\frac{3L}{4} < x < L$
Top wall $t^* > 0$, $y = L$, $0 < x < L$:	$u = v = 0$	$\frac{\partial T}{\partial y} = 0$ for $0 < x < \frac{L}{4}$ $T = T_c$ for $\frac{L}{4} < x < \frac{3L}{4}$ $\frac{\partial T}{\partial y} = 0$ for $\frac{3L}{4} < x < L$

TABLE II. Thermophysical properties of $H_2O, C_2H_6O_2$ and Al_2O_3 [31,54–59]

Property	H_2O	$C_2H_6O_2$	Al_2O_3
$\rho(kgm^{-3})$	997·1	1117·48	3970
$C_p(Jkg^{-1}K^{-1})$	4179	2382·1	765
$k(Wm^{-1}k^{-1})$	0·613	0·2492	40
$\beta(k^{-1})$	21×10^{-5}	57×10^{-5}	0.85×10^{-5}
$\sigma(\Omega^{-1}m^{-1})$	0.05	$1\cdot07\times10^{-8}$	1×10^{-10}
$\mu(Pa.s)$	$8\cdot9\times10^{-4}$	0·022	-
Pr	6·2	210·3	-

$$\frac{\partial V}{\partial t}+U\frac{\partial V}{\partial X}+V\frac{\partial V}{\partial Y}=-\left(\frac{\rho_f}{\rho_{nf}}\right)\frac{\partial P}{\partial Y}+\left(\frac{\nu_{nf}}{\nu_f}\right)\frac{1}{Re}\left[\frac{\partial^2 V}{\partial X^2}+\frac{\partial^2 V}{\partial Y^2}\right]+\left(\frac{\sigma_{nf}}{\sigma_f}\right)\left(\frac{\rho_f}{\rho_{nf}}\right)\frac{Ha^2}{Re}\left(U\sin\Theta\cos\Theta-V\cos^2\Theta\right)-\left(\frac{\nu_{nf}}{\nu_f}\right)\frac{1}{Re\,Da}V+\frac{(\rho\beta)_{nf}}{\rho_{nf}\beta_f}Ri\,\theta \tag{19}$$

$$\frac{\partial\theta}{\partial t}+U\frac{\partial\theta}{\partial X}+V\frac{\partial\theta}{\partial Y}=\left(\frac{\alpha_{nf}}{\alpha_f}\right)\frac{1}{Re\,Pr}\left[\frac{\partial^2\theta}{\partial X^2}+\frac{\partial^2\theta}{\partial Y^2}\right]+\left(\frac{\alpha_{nf}}{\alpha_f}\right)\frac{Q}{Re\,Pr}\theta+\left(\frac{\mu_{nf}}{\mu_f}\right)\left(\frac{(\rho C_p)_f}{(\rho C_p)_{nf}}\right)\frac{Ec}{Da\,Re}\left(U^2+V^2\right)+\left(\frac{\sigma_{nf}}{\sigma_f}\right)\left[\frac{(\rho C_p)_f}{(\rho C_p)_{nf}}\right]\frac{Ha^2\,Ec}{Re}V^2+\left(\frac{\mu_{nf}}{\mu_f}\right)\left(\frac{(\rho C_p)_f}{(\rho C_p)_{nf}}\right)\frac{Ec}{Re}\left(2\left(\frac{\partial U}{\partial X}\right)^2+2\left(\frac{\partial V}{\partial Y}\right)^2+\left(\frac{\partial V}{\partial X}+\frac{\partial U}{\partial Y}\right)^2\right) \tag{20}$$

The non-dimensional pertinent parameters arising in Eqns. (18)-(20) are tabulated in Table III and the dimensionless form of the initial and boundary conditions are tabulated in Table IV. The local and mean heat transfer rates are given by the subsequent expressions:

$$Nu=-\frac{k_{nf}}{k_f}\left(\frac{\partial\theta}{\partial Y}\right)_{Y=0} \tag{21}$$

$$Nu_{avg}=\int_0^1 Nu\,dx \tag{22}$$

TABLE III. The non-dimensional pertinent parameters

Re	$\frac{V_f}{U_0 L}$
Gr	$\frac{g\beta_f(T_h-T_c)L^3}{\nu_f^2}$
Pr	$\frac{\nu_f}{\alpha_f}$
Ha	$B_0 L\sqrt{\frac{\sigma_f}{\mu_f}}$
Ec	$\frac{U_0^2}{(C_p)_f(T_h-T_c)}$
Ri	$\frac{Gr}{Re^2}$
Q	$\frac{Q_0 L^2}{(\rho C_p)_{nf}\alpha_{nf}}$
Da	$\frac{K}{L^2}$

III. MAC COMPUTATION AND VALIDATION

The momentum and temperature equations (18) – (20) with the associated dimensionless initial and boundary conditions (Table IV) are solved by adopting the MAC technique. The pressure distribution is computed by using the continuity equation (17). The numerical outcomes are implemented in terms of velocity components (U, V). Although viscous flow is considered, in the MAC technique, viscosity is not essential for the numerical simulations. In the finite-difference discretization, the cell boundaries are labeled with half-integer values. However, the marker cells are not used in the computation. In this section, the numerical discretization technique is discussed in detail. According to the weak conservation form of the time-dependent two-dimensional Navier-Stokes equations and temperature equation as described by eqns. (18) – (20), the following grid meshing procedure is used at the center of a cell:

$$U_{i-\frac{1}{2},j}=\frac{1}{2}\left(U_{i-1,j}+U_{i,j}\right) \tag{23}$$

The subscripts i and j in the previous equality represent the space coordinates in the X and Y directions, respectively.

Apply Eq. (23) into the X-direction momentum conservation Eqn. (18) to obtain the following:

$$\frac{\partial(UU)}{\partial X}=\frac{\left(\frac{1}{2}\left(U_{i,j}+U_{i+1,j}\right)\right)^2-\left(\frac{1}{2}\left(U_{i-1,j}+U_{i,j}\right)\right)^2}{\Delta X} \tag{24}$$

$$\frac{\partial(UV)}{\partial Y}=\frac{\frac{1}{4}\left(U_{i,j}+U_{i,j+1}\right)\left(V_{i,j}+V_{i+1,j}\right)}{\Delta Y}-\frac{\frac{1}{4}\left(U_{i,j}+U_{i,j-1}\right)\left(V_{i,j-1}+V_{i+1,j-1}\right)}{\Delta Y} \tag{25}$$

TABLE IV. The dimensionless form of the initial and boundary conditions

Initial condition $t \leq 0,\ 0 \leq X \leq 1,\ 0 \leq Y \leq 1$:	$U = V = 0$	$\theta = 0$
Left wall $t > 0,\ X = 0,\ 0 < Y < 1$:	$U = V = 0$	$\frac{\partial \theta}{\partial X} = 0$ for $0 < Y < \frac{1}{4}$ $\theta = 1$ for $\frac{1}{4} < y < \frac{3}{4}$ $\frac{\partial \theta}{\partial X} = 0$ for $\frac{3}{4} < Y < 1$
Right wall $t > 0,\ X = 1,\ 0 < Y < 1$:	$U = V = 0$	$\frac{\partial \theta}{\partial X} = 0$ for $0 < Y < \frac{1}{4}$ $\theta = 1$ for $\frac{1}{4} < y < \frac{3}{4}$ $\frac{\partial \theta}{\partial X} = 0$ for $\frac{3}{4} < Y < 1$
Bottom wall $t > 0,\ Y = 0,\ 0 < X < 1$:	$U = V = 0$	$\frac{\partial \theta}{\partial Y} = 0$ for $0 < X < \frac{1}{4}$ $\theta = 0$ for $\frac{1}{4} < X < \frac{3}{4}$ $\frac{\partial \theta}{\partial Y} = 0$ for $\frac{3}{4} < X < 1$
Top wall $t > 0,\ Y = 1,\ 0 < X < 1$:	$U = V = 0$	$\frac{\partial \theta}{\partial Y} = 0$ for $0 < x < \frac{1}{4}$ $\theta = 0$ for $\frac{1}{4} < x < \frac{3}{4}$ $\frac{\partial \theta}{\partial Y} = 0$ for $\frac{3}{4} < X < 1$

For second order derivatives, the following central difference formula is used,

$$\nabla^2 U = \frac{\partial^2 U}{\partial X^2} + \frac{\partial^2 U}{\partial Y^2} \tag{26}$$

$$\nabla^2 U = \frac{U_{i-1,j} - 2U_{i,j} + U_{i+1,j}}{\Delta X^2} + \frac{U_{i,j-1} - 2U_{i,j} + U_{i,j+1}}{\Delta Y^2} \tag{27}$$

Next, Eq. (23) is applied into the Y-direction momentum conservation Eqn. (19) to obtain the following:

$$\frac{\partial (VU)}{\partial X} = \frac{\frac{1}{2}\left(U_{i,j+1} + U_{i,j}\right)\left(V_{i,j} + V_{i+1,j}\right)}{\Delta X} - \frac{\frac{1}{4}\left(U_{i-1,j+1} + U_{i-1,j}\right)\left(V_{i,j} + V_{i-1,j}\right)}{\Delta X} \tag{28}$$

$$\frac{\partial (VV)}{\partial Y} = \frac{\left(\frac{1}{2}\left(V_{i,j+1} + V_{i,j}\right)\right)^2 - \left(\frac{1}{2}\left(V_{i,j-1} + V_{i,j}\right)\right)^2}{\Delta Y} \tag{29}$$

The central difference formula for the Laplacian operator is provided by:

$$\nabla^2 V = \frac{\partial^2 V}{\partial X^2} + \frac{\partial^2 V}{\partial Y^2} \tag{30}$$

$$\nabla^2 V = \frac{V_{i-1,j} - 2V_{i,j} + V_{i+1,j}}{\Delta X^2} + \frac{V_{i,j-1} - 2V_{i,j} + V_{i,j+1}}{\Delta Y^2} \tag{31}$$

The X-momentum equation's discretization approach is described as follows:

$$U^{n+1} = U^n + dt\left[-\left(U\frac{\partial U}{\partial X} + V\frac{\partial U}{\partial Y}\right) + \frac{1}{Re}\left(\frac{\partial^2 U}{\partial X^2} + \frac{\partial^2 U}{\partial Y^2}\right)\right] + dt\left[-\frac{1}{Re\,Da}U + \frac{Ha^2}{Re}\left(V\sin\Theta\cos\Theta - U\sin^2\Theta\right)\right] \tag{32}$$

The Y-momentum equation requires a minor adjustment with the addition of a new term, and becomes:

$$V^{n+1} = V^n + dt\left[-\left(U\frac{\partial V}{\partial X} + V\frac{\partial V}{\partial Y}\right) + \frac{1}{Re}\left(\frac{\partial^2 V}{\partial X^2} + \frac{\partial^2 V}{\partial Y^2}\right)\right] + dt\left[-\frac{1}{Re\,Da}V + Ri\theta + \frac{Ha^2}{Re}\left(U\sin\Theta\cos\Theta - V\cos^2\Theta\right)\right] \tag{33}$$

It is important to note that the temperature term θ is co-located with the velocity before being used in the previous equation to accommodate the staggered grid. The pressure term is considered as:

$$\frac{\nabla^2 U}{dt} = \nabla^2 P \tag{34}$$

The discretized temperature equation required to move to the next time level (θ^{n+1}) which is obtained as follows:

$$\theta^{n+1} = \theta^n + dt\left(-\left(U\frac{\partial\theta}{\partial X} + V\frac{\partial\theta}{\partial Y}\right) + \frac{1}{RePr}\left(\frac{\partial^2\theta}{\partial X^2} + \frac{\partial^2\theta}{\partial Y^2} + Q\theta\right)\right) + dt\left(\frac{Ha^2 Ec}{Re}V^2\right) + dt\left(\frac{Ec}{Re}\left(\frac{1}{Da}\left(U^2 + V^2\right)\right)\right) + dt\left(\frac{Ec}{Re}\left(2\left(\frac{\partial U}{\partial X}\right)^2 + 2\left(\frac{\partial V}{\partial Y}\right)^2 + \left(\frac{\partial V}{\partial X} + \frac{\partial U}{\partial Y}\right)^2\right)\right) \tag{35}$$

In the absence of thermophysical properties of the nanofluid, heat source/sink, ohmic heating, inclined magnetic field, viscous dissipation, and in the presence of radiation, with modifications in the geometry, initial and boundary conditions, the current model is equated with some of the results presented by Khan et al.[28] Figure 2 displays the comparison of the streamlines and isotherms computed from the current MAC code with the earlier solutions of Khan et al.[28] Excellent correlation is attained and it confirms the accuracy of the present MAC code.

IV. RESULT AND DISCUSSION

The transport characteristics for laminar mixed convection of magnetohydrodynamic γ–$Al_2O_3 - H_2O$ and γ–$Al_2O_3 - C_2H_6O_2$ nanofluids flow inside a square porous cavity with Joule heating, inclined magnetic field, viscous dissipation, and heat sink/source effects have been computed by adopting the MAC scheme. Extensive visualization of the solutions is presented in Figure [3-14]. The non-dimensional control parameters values deployed in the computations are selected from the literature[31,42,45,49] to physically represent real flows. The ranges prescribed for the pertinent parameters are as follows: Prandtl number ($C_2H_6O_2 = 210.3$ & $H_2O = 6.2$), Darcy number ($10^{-3} < Da < 10^{-1}$), Hartmann number ($10 < Ha \leq 100$), Reynolds number ($2 \leq Re \leq 10$), Richardson number ($10^{-2} \leq Ri \leq 10^{2}$), Eckert (dissipation) number ($0 \leq Ec \leq 1$), nanofluid volume fraction ($0 \leq \Phi \leq 0.05$) and volumetric heat generation/absorption coefficient ($-6 \leq Q \leq 6$). Throughout the simulations, the following default values are deployed: $Da = 10^{-3}$, $Q = -6$, $\Phi = 0.05$, $Ec = 0.3$, $Ri = 1$, $Re = 2$, and $Ha = 10$, unless otherwise specified. Figures [3–14] depict the influence of these parameters on local heat transfer rate, isotherms, and streamlines. In addition, Tables (V-VII) are presented for mean Nusselt number distribution.

A. Streamlines variation with Hartmann number

Figure 3 portrays the inclined magnetic field effect through the Hartmann number on streamlines contours for γ–$Al_2O_3 - H_2O$ and γ–$Al_2O_3 - C_2H_6O_2$ nanofluids. In general, the Hartmann number exerts a critical influence on the momentum and thermal convection process. The magnetic field inclination (Θ) features in both X and Y-momentum equations. It appears in the term, $\frac{\sigma_{nf}B_0^2}{\rho_{nf}}\left(V\sin\Theta\cos\Theta - U\sin^2\Theta\right)$ in the X-momentum Eqn. (18) and $\frac{\sigma_{nf}B_0^2}{\rho_{nf}}\left(U\sin\Theta\cos\Theta - V\cos^2\Theta\right)$ in the Y-momentum Eqn. (19). The shape and strength of the circulating cells of the streamlines are modified substantially for both nanofluids as Ha increases. A single right circulation cell and a single left circulation cell are identified in the case of the γ–$Al_2O_3 - H_2O$ nanofluid. Instead, double right circulation cells and double left circulation cells are identified in case of the γ–$Al_2O_3 - C_2H_6O_2$ nanofluid. This indicates that the fluid motion is slower (i.e. deceleration in the circulation is induced) in the γ–$Al_2O_3 - C_2H_6O_2$ nanofluid case compared to γ–$Al_2O_3 - H_2O$ nanofluid case. The circulation cells are reduced in all cases as the enhancement in the magnetic field has the tendency to increase the strength of the Lorentz force which damps the flow. Magnification in the Lorentz force causes a decrease in fluid mass displacement and therefore the expansion of the circulation cells diminishes. When strength of the magnetic field is amplified, the density of the streamlines along the walls decreases, indicating that the velocity decelerates in these areas. In addition, as the Hartmann number is increased, the center of the circulation cells has migrated towards the warmer regions. In other words, increasing the Hartmann number causes eddies to stretch along the vertical direction.

B. Effects of Darcy numbers on streamlines

In any flow domain, the impact of porous medium implies the distribution of solid matrix fibers throughout the region. This matrix structure modifies the heat transfer characteristics and particularly affects the fluid flow characteristics. The porous medium permeability is represented here by permeability (K) which features in the Darcy number (Da). The Darcy number occurs in both the primary and secondary momentum equations (18) and (19) as linear Darcy drag force terms, viz, $-\frac{\nu_{nf}}{\nu_f}\frac{1}{Re\,Da}U$ and $-\frac{\nu_{nf}}{\nu_f}\frac{1}{Re\,Da}V$. Permeability of the porous medium is evaluated using physically viable values of Darcy number ($10^{-3} \leq Da \leq 10^{-1}$), with the fixed value of other pertinent parameters. Figure 4 portrays the Darcy number influence on streamlines distribution of γ–$Al_2O_3 - H_2O$ and γ–$Al_2O_3 - C_2H_6O_2$ nanofluids. As seen, the circulation cells are formed at the central (core) zone of the enclosure in the γ–$Al_2O_3 - H_2O$ nanofluid case and the circulation cells are split into two eddies at top and bottom of the cavity in γ–$Al_2O_3 - C_2H_6O_2$ case. Increasing values of Darcy number have the tendency to upsurge the magnitudes of the inner circulation cells in γ–$Al_2O_3 - H_2O$ nanofluid case and the inner circulation cells are expanded to the middle of the cavity in γ–$Al_2O_3 - C_2H_6O_2$ case. It is an evident that the fluid velocity increases (i.e. internal flow acceleration is induced) at the central zone of the cavity with magnifying values of Darcy

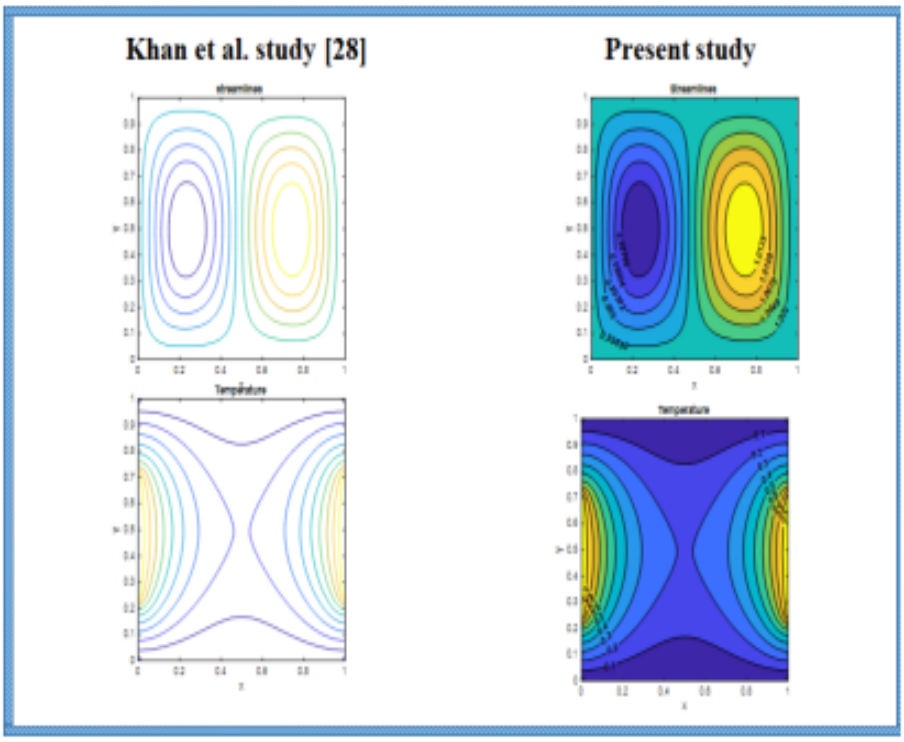

FIG. 2. Comparison contour plots with $Pr = 0.71, Re = 10, Nr = 1, Gr = 10^3, Da = 10^{-2}$.

number.

C. Effects of heat source/sink on isotherms

Figure 5 portrays the impact of heat sink/source (Q) on the isotherms for $\gamma - Al_2O_3 - H_2O$ and γ–$Al_2O_3 - C_2H_6O_2$ nanofluids. It has a substantial role in the energy transmission characteristics inside the cavity. The isotherm distributions evolve considerably due to the changes in Q. The characteristics of heat absorption/generation parameter on the isotherms contours of γ–$Al_2O_3 - H_2O$ nanofluid are presented in Figure 5(A). It is to be noted that $Q > 0$ indicates the internal heat generation whereas $Q < 0$ represents the internal absorption of heat. As seen, in the case of heat sink $(Q = -6)$, the impact of the hot slits is dominated by the cool slits and the center region is cooled. In the absence of heat sink/source $(Q = 0)$, the impact of the hot slits is higher in the center region of the cavity. The impact of the hot slits is predominantly visible in the center region when the heat source $(Q = 6)$ is present. As a result, the energy transmission is notably augmented for increasing the heat source parameter values. Though this impact is not particularly prominent in the γ–$Al_2O_3 - C_2H_6O_2$ nanofluid, the magnitudes of the circulation cells are slightly increased for higher heat source parameter values. Therefore, the influence of the heat absorption/generation parameter is more dominant in the γ–$Al_2O_3 - H_2O$ nanofluid compared to γ–$Al_2O_3 - C_2H_6O_2$ nanofluid.

D. Effects of nanofluid volume fraction on streamlines and isotherms

Velocity distribution of the considered nanofluids is not notably influenced with nanoparticle volume fraction. Figure 6 illustrates that the streamlines of γ–$Al_2O_3 - H_2O$ and γ–$Al_2O_3 - C_2H_6O_2$ nanofluids are almost invariant as the volume fraction upsurges. It is noted that in the γ–$Al_2O_3 - H_2O$ nanofluid case, flow circulation characterized by circulation cells form in the center of the enclosure. In the γ–$Al_2O_3 - C_2H_6O_2$ case, the circulation cells are divided in two parts at the top and bottom of the enclosure.

Figure 7 demonstrates the influence of volume fraction (Φ) on isotherms for γ–$Al_2O_3 - H_2O$ and γ–$Al_2O_3 - C_2H_6O_2$ nanofluids. The numerical results of this study demonstrate that the energy transmission features of the considered nanofluids is improved considerably with the nanoparticles volume fraction. The volume fraction factor is essential in understanding how the nanoparticles modify the energy transmission of nanoliquid from the hot wall to the cold wall. As the volume fraction grows, uneven and random particle motions enhance the energy exchange rates in the fluid and, as a result, an improvement in the thermal distribution of the nanofluids are observed. Figures 7(A-I) and 7(B-I) elucidate the characteristics of isotherms of H_2O and $C_2H_6O_2$ fluids without any nanoparticles $(\Phi = 0)$. It is observed that $C_2H_6O_2$ nanofluid has higher heat transfer than H_2O. 3% and 5% suspensions of γ–Al_2O_3 nanoparticles in the base-fluid water are presented in Figures 7(A-II) and 7(A-III), respectively. Figures 7(B-II) and 7(B-III) illustrate the features of isotherms

with 3% and 5% of γ–Al_2O_3 nanoparticles suspension into the base-fluid $C_2H_6O_2$. In the γ–$Al_2O_3 - H_2O$ nanofluid case, the circulation cells migrate to the top and bottom walls, so the heat is transferred from the left to right wall more effectively. In γ–$Al_2O_3 - C_2H_6O_2$ case, heat is transferred throughout the cavity. It is noticed that when the nanoparticle volume fraction is magnified, the temperature enhancement in the center region is more amplified in the case of the γ–$Al_2O_3 - H_2O$ nanofluid compared to γ–$Al_2O_3 - C_2H_6O_2$ nanofluid. However, the energy transmission efficiency of γ–$Al_2O_3 - C_2H_6O_2$ nanofluid is higher than γ–$Al_2O_3 - H_2O$ nanofluid.

E. Effects of Richardson numbers on streamlines and isotherms

Figure 8 explores the forced (I), mixed (II), and natural (III) convective flow aspects for both γ–$Al_2O_3 - H_2O$ and γ–$Al_2O_3 - C_2H_6O_2$ nanofluids. The Richardson number (Ri) plays a significant part in manipulating the convective transport within the enclosure. Smaller values of Richardson number (Ri) correspond to the forced convection flow $(Ri < 1)$, $Ri = 1$ characterizes the mixed convection flow and higher values of Richardson number imply the natural convection flow $(Ri > 1)$. The Richardson number is included in the single thermal buoyancy term $\frac{(\rho\beta)_{nf}}{\rho_{nf}\beta_f} Ri\ \theta$ added in the Y-direction momentum equation (19). Figure 8(I) illustrates the evolution in streamlines for γ–$Al_2O_3 - H_2O$ and γ–$Al_2O_3 - C_2H_6O_2$ nanofluids for forced convective flow i.e. $Ri = 0.01$. In the γ–$Al_2O_3 - H_2O$ nanofluid case, more circulation cells are synthesized in the vicinity of the right wall with strong circulation in the center zone of the enclosure, whereas in the γ–$Al_2O_3 - C_2H_6O_2$ nanofluid case, the circulation cells are split in two distinct groups at the bottom and top of enclosure and no significant flow is computed at the center of the enclosure. The shapes of the circulation cells do not change when the value of Ri is increased from 0·01 to 1 for either nanofluids. That is, the forced convective flow behavior is sustained even for the mixed convective flow mode. When $Ri = 100$, the magnitudes of inner circulation cells are increased and thereby it is noticed that the velocity of the fluid increases in the cavity as shown in Figure 8(III) for both nanofluid cases. The magnitude of streamlines is slightly higher in γ–$Al_2O_3 - H_2O$ nanofluid compared to γ–$Al_2O_3 - C_2H_6O_2$ nanofluid. This demonstrates that γ–$Al_2O_3 - H_2O$ nanofluid has better flow characteristics than γ–$Al_2O_3 - C_2H_6O_2$ nanofluid.

Figure 9 illustrates the isotherms contour plots for γ–$Al_2O_3 - H_2O$ and γ–$Al_2O_3 - C_2H_6O_2$ nanofluids. In γ–$Al_2O_3 - H_2O$ case, more heat is transferred near the right and left walls but in the γ–$Al_2O_3 - C_2H_6O_2$ case, heat is transferred throughout the cavity. The impact of Richardson number is not significant on the isotherms for the considered nanofluids.

F. Effects of Reynolds numbers on streamlines and isotherms

Figure 10 depicts the streamline distributions in the enclosure for varying the Reynolds number (Re) with γ–$Al_2O_3 - H_2O$ and γ–$Al_2O_3 - C_2H_6O_2$ nanofluids. The relative contribution of inertial forces to viscous forces is represented by the Reynolds number. The Reynolds number is a dimensionless number which is used to classify the fluid flow. It is well-known that the influence of viscosity is important in controlling velocities or flow patterns. As a result, the Reynolds number plays a predominant role on the transport characteristics of viscous fluids. In Figure 10A, a single primary recirculation cell is observed in case of γ–$Al_2O_3 - H_2O$ nanofluid and circulation cells are fragmented into two parts and more circulations are formed at the bottom and top of the cavity for γ–$Al_2O_3 - C_2H_6O_2$ nanofluid. The circulations cells at the center region of the enclosure are decreased with higher Reynolds number values. When increasing the Reynolds number values from $Re = 2$ to $Re = 5$, the inner most circulation cell shrinks at the center and moves closer to the top and bottom of the cavity in case of γ–$Al_2O_3 - H_2O$ nanofluid. When Re=10, a peanut-shell shaped structure is formed, and the inner circulation cells are broken. This indicates that the velocity of the nanofluid is decreased at the center region of the cavity. However, the density of the circulation cells near the bottom and top walls are increased for higher Reynolds number values. This implies that the flow near the horizontal walls is accelerated with higher Reynolds number values. With increment in Reynolds number from $Re = 2$ to $Re = 5$, the outer most circulations cells at the center region of the enclosure are contracted in the case of γ–$Al_2O_3 - C_2H_6O_2$ nanofluid. This indicates that at the vertical walls side of the enclosure, fluid velocity is diminished. When $Re = 10$, the left circulation cells are formed at the top and bottom of the enclosure separately and the outer most right circulation cell is further depleted in size and forms a peanut-shell shaped structure. This suggests that the velocity of the nanofluid is decreased at the center region and increased near the bottom and top walls of the cavity. The streamline patterns overall indicate that the velocity of γ–$Al_2O_3 - H_2O$ nanofluid in the enclosure is higher than that of γ–$Al_2O_3 - C_2H_6O_2$ nanofluid.

Figure 11 represents the isotherms of γ–$Al_2O_3 - H_2O$ and γ–$Al_2O_3 - C_2H_6O_2$ nanofluids inside the cavity with different Reynolds number values. The heat transfer characteristics of γ–$Al_2O_3 - H_2O$ nanofluid for various Reynolds number values are presented in Figure 11(A). As seen in Figure 11(A-I), when $Re = 2$, the energy transmission within the cavity is suppressed. The impact of the hot slits and cold slits are more pronounced in their neighborhoods. When $Re = 5$, the impact of the hot slits dominates the impact of the cold slits at the center region and greater heat transfer is observed as illustrated in Figure 11(A-II). When $Re = 10$, the impact of the hot slits is predominant at the center region which is demonstrated in Figure 11(A-III). The results reveal that the energy transmission is significantly enhanced for magnifying the Reynolds number i.e. with greater inertial force relative to viscous force in the regime. The heat transfer character-

istics of γ–$Al_2O_3 - C_2H_6O_2$ nanofluid is presented in Figure 11(B). It is noticed that the impact of the cold slits is considerably decreased, and the energy transmission is amplified for augmenting the Reynolds number. The impact of the hot slits is more pronounced with higher Reynolds number values. It is observed that the energy transmission efficiency of γ–$Al_2O_3 - C_2H_6O_2$ nanofluid is higher than γ–$Al_2O_3 - H_2O$ nanofluid.

G. Characteristics of Nusselt number distribution

The impact of volume fraction on local heat transfer rate is displayed in Figure 12. The local Nusselt number profiles are enhanced with magnifying volume fraction of nanoparticles. More variations are noticed in the case of γ–$Al_2O_3 - C_2H_6O_2$ nanoliquid compared to γ–$Al_2O_3 - H_2O$ nanoliquid. The characteristics of mean heat transfer rate for various volume fractions are presented in Table *V*. As observed, obviously there is a very substantial difference in the heat transfer rate computed with different base-fluids (H_2O & $C_2H_6O_2$). In the absence of nanoparticles, there is a 382 · 89% difference in the mean heat transfer rate of γ–$Al_2O_3 - H_2O$ and γ–$Al_2O_3 - C_2H_6O_2$ nanofluids. The heat transfer rate of γ–$Al_2O_3 - C_2H_6O_2$ nanofluid is higher than γ–$Al_2O_3 - H_2O$ nanofluid. When 3% of γ–Al_2O_3 nanoparticles are suspended into H_2O and $C_2H_6O_2$ base-fluids, the mean heat transfer rate of γ–$Al_2O_3 - C_2H_6O_2$ nanofluid is 410 · 91% higher than that of γ–$Al_2O_3 - H_2O$ nanofluid. When 5% of γ–Al_2O_3 nanoparticles are suspended into H_2O and $C_2H_6O_2$ base-fluids, the difference in the mean heat transfer rate between γ–$Al_2O_3 - H_2O$ and γ–$Al_2O_3 - C_2H_6O_2$ nanofluids is increased to 450 · 43%. In addition, compared to the base-fluids H_2O and $C_2H_6O_2$, the γ–$Al_2O_3 - H_2O$ and γ–$Al_2O_3 - C_2H_6O_2$ nanofluids have higher average heat transfer rates. Hence, the presence of nanoparticles considerably boosts the energy transmission characteristics of the base-fluids.

The heat sink/source parameter's impact on local heat transfer rate is presented in Figure 13. The local Nusselt number profiles are enhanced with magnifying heat source values ($Q = +6$) whereas they are suppressed with increasing heat sink parameter values ($Q = -6$). The case of $Q = 0$ implies an absence of either heat source or sink. Greater variations are computed in the case of γ–$Al_2O_3 - H_2O$ nanofluid compared to γ–$Al_2O_3 - C_2H_6O_2$ nanofluid. The characteristics of mean heat transfer rate for various heat sink/source parameter values are illustrated in Table VI. In the presence of heat sink, the average heat transfer rate of γ–$Al_2O_3 - H_2O$ nanofluid is 450 · 43% lower than γ–$Al_2O_3 - C_2H_6O_2$ nanofluid. In the absence of heat sink/source, the average heat transfer rate of γ–$Al_2O_3 - C_2H_6O_2$ nanofluid is 305 · 85% higher than that of γ–$Al_2O_3 - H_2O$ nanoliquid. In the presence of heat source, the average heat transfer rate of γ–$Al_2O_3 - C_2H_6O_2$ nanofluid is 194 · 92% higher than γ–$Al_2O_3 - H_2O$ nanofluid. Therefore, there is a huge variation in the increment of the mean heat transfer rate for the considered nanoliquids with modification in heat absorption/generation within the enclosure.

The impact of various Eckert number values on local and mean heat transfer rates is presented in Figure 14 and Table VII, respectively. The results reveals that a slight enhancement is observed for magnifying the Eckert number values, indicating that viscous heating and Joule heating do exert an influence on the heat transfer characteristics.

V. CONCLUSIONS

Inspired by the emerging applications in magnetic nanomaterials processes and hybrid electromagnetic nanofluid fuel cells, the current work has presented a numerical investigation of the combined effects of viscous dissipation and ohmic heating on magnetohydrodynamic (MHD) mixed convection γ–$Al_2O_3 - H_2O$ and γ–$Al_2O_3 - C_2H_6O_2$ nanofluids transport inside a cavity under the impact of inclined magnetic field. The Tiwari-Das nanoscale model is adopted with different correlation models deployed for thermal conductivity, dynamic viscosity, and effective Prandtl number formulations for the thermophysical properties of nanofluids. At the center of the right and left walls of the enclosure, hot slits are included. At the center of the top and bottom walls, cold slits are located. Other portions of the cavity are considered as adiabatic. The transformed dimensionless momentum and energy equations are solved by applying a stable, accurate, finite difference MAC method. Validations with earlier study are included. The key observations from the simulations are summarized as follows:

1. As the magnetic field strength is increased (i.e. with increasing Hartmann number), the density of the streamlines along the walls decreases, indicating that the velocity diminishes in these areas. In addition, as the Hartmann number is increased, the center of the circulation cell is observed to migrate towards warmer regions inside the enclosure.

2. Increasing values of the Darcy number (i. e. for greater permeability of the porous medium), has the tendency to increase the magnitudes of the inner circulation cells in the γ–$Al_2O_3 - H_2O$ nanofluid case and the inner circulation cells are expanded to the central zone of the enclosure in the γ–$Al_2O_3 - C_2H_6O_2$ case. This indicates that the flow acceleration and circulation intensification is generated at the middle of the enclosure with increment in the Darcy number.

3. Heat transfer is notably increased with an increment in the heat source parameter; whereas it is suppressed with heat sink parameter. The impact of the heat absorption/generation parameter is more dominant in γ–$Al_2O_3 - H_2O$ nanofluid case compared to γ–$Al_2O_3 - C_2H_6O_2$ nanofluid case.

4. The heat transfer rate of γ–$Al_2O_3 - C_2H_6O_2$ nanofluid is markedly higher than γ–$Al_2O_3 - H_2O$ nanofluid. When 5% of γ–Al_2O_3 nanoparticles are suspended into H_2O and $C_2H_6O_2$ base-fluids, the difference in the mean heat transfer rate of γ–$Al_2O_3 - H_2O$ and γ–$Al_2O_3 - C_2H_6O_2$ nanofluids is increased to 450 · 43%.

TABLE V. Mean heat transfer rate variations with different values of volume fraction parameter

Pertinent Parameter	γ-$Al_2O_3 - H_2O$	γ-$Al_2O_3 - C_2H_6O_2$
$\Phi = 0.00$	1.325954311011331	6.403021254584748
$\Phi = 0.03$	1.499236907611164	7.659768142773325
$\Phi = 0.05$	1.665814975702705	9.169209316562142

TABLE VI. Mean heat transfer rate variations with different values of heat source/sink parameter

Pertinent Parameter	γ-$Al_2O_3 - H_2O$	γ-$Al_2O_3 - C_2H_6O_2$
$Q = -6$	1.665814975702705	9.169209316562142
$Q = 0$	2.283827139476982	9.268971954320264
$Q = 6$	3.177005080214399	9.369799598102119

5. The local Nusselt number profiles are enhanced for magnifying the heat source parameter values but depleted with greater heat sink parameter values. More significant modifications are observed in the case of γ-$Al_2O_3 - H_2O$ nanoliquid. When the heat source is present, the average heat transfer rate of γ-$Al_2O_3 - C_2H_6O_2$ nanofluid is $194 \cdot 92\%$ higher than that of γ-$Al_2O_3 - H_2O$ nanofluid, indicating an impressive thermal enhancement with the existence of heat source.

The present research has demonstrated some fascinating characteristics of forced, natural and mixed convective magneto-nanofluid flow inside a porous medium enclosure using different base-fluids with a single type of nanoparticle (γ-alumina). The MAC algorithm has been shown to be very precise and adaptable for simulating such problems of relevance to electroconductive nanofluid materials processing operations and hybrid magnetic nano-fuel cells.

ACKNOWLEDGMENTS

The second author (R. Sivaraj) is thankful to the Ministry of Education, United Arab Emirates for the financial assistance to complete this research work.

CONFLICTS OF INTEREST

The authors have no conflicts to disclose.

REFERENCES

[1]S. U. Choi and J. A. Eastman, "Enhancing thermal conductivity of fluids with nanoparticles," (1995).
[2]M. Sankar, B. Jang, and Y. Do, "Numerical study of non-darcy natural convection from two discrete heat sources in a vertical annulus," Journal of Porous Media **17**, 373–390 (2014).
[3]D. D. Dixit and A. Pattamatta, "Natural convection heat transfer in a cavity filled with electrically conducting nano-particle suspension in the presence of magnetic field," Physics of Fluids **31**, 023302 (2019).
[4]A.Bendaraa, M. M. Charafi, and A. Hasnaoui, "Numerical study of natural convection in a differentially heated square cavity filled with nanofluid in the presence of fins attached to walls in different locations," Physics of Fluids **31**, 052003 (2019).
[5]M.Hamid, Z. H. Khan, W. A. Khan, and R. U. Haq, "Natural convection of water-based carbon nanotubes in a partially heated rectangular fin-shaped cavity with an inner cylindrical obstacle," Physics of Fluids **31**, 103607 (2019).
[6]K. S. Arjun and K. Rakesh, "Heat transfer in magnetohydrodynamic nanofluid flow past a circular cylinder," Physics of Fluids **32**, 045112 (2020).
[7]C.-C. Cho, "Natural convection of cu-water nanofluid in enclosed cavity with porous effect and wavy surface based on energy-flux-vector visualization method," Physics of Fluids **32**, 103607 (2020).
[8]M. S. Alnarabiji and M. M. Husein, "Application of bare nanoparticle-based nanofluids in enhanced oil recovery," Fuel **267**, 117262 (2020).
[9]B. V.Pushpa, M. Sankar, and F. Mebarek-Oudina, "Buoyant convective flow and heat dissipation of cu-h2o nanoliquids in an annulus through a thin baffle," Journal of Nanofluids **10**, 292–304 (2021).
[10]M.Sankar, N. K. Reddy, and Y. Do, "Conjugate buoyant convective transport of nanofluids in an enclosed annular geometry," Scientific Reports **11**, 17122 (2021).
[11]R. Sivaraj and S. Banerjee, "Transport properties of non-newtonian nanofluids and applications," The European Physical Journal Special Topics **230**, 1167–1171 (2021).
[12]G. S. Sokhal, "Numerical study on the behaviour of al2o3/water nanofluid at multiple flows and concentration," Materials Today: Proceedings **37**, 3296–3300 (2021).
[13]K. Y. Paranjpe, "Alpha, beta and gamma alumina as a catalyst -a review," Pharma Innovation International Journal **6**, 236–238 (2017).
[14]H. S. Moghaieb, H. Abdel-Hamid, M. H. Shedid, and A. Helali, "Engine cooling using al2o3/water nanofluids," Applied Thermal Engineering **115**, 152–159 (2017).
[15]I. Nowrouzi, A. K. Manshad, and A. H. Mohammadi, "Effects of tio2, mgo and γ-al2o3 nano-particles on wettability alteration and oil production under carbonated nano-fluid imbibition in carbonate oil reservoirs," Fuel **259**, 116110 (2020).
[16]M. S. Radwan, H. E. Saleh, Y. A. Attai, and M. S. Elsherbiny, "On heat transfer enhancement in diesel engine cylinder head using γ-al2o3/water nanofluid with different nanoparticle sizes," Advances in Mechanical Engineering **12**, 1687814019897507 (2020).
[17]N. V. Ganesh, S. Javed, Q. M. Al-Mdallal, R. Kalaivanan, and A. J. Chamkha, "Numerical study of heat generating γ al2o3– h2o nanofluid inside a square cavity with multiple obstacles of different shapes," Heliyon **6**, e05752 (2020).
[18]F. García, C. Treviño, J. Lizardi, and L. Martínez-Suástegui, "Numerical study of buoyancy and inclination effects on transient mixed convection in a channel with two facing cavities with discrete heating," International Journal of Mechanical Sciences **155**, 295–314 (2019).
[19]A. A. Arani, S. M. Sebdani, M. Mahmoodi, A. Ardeshiri, and M. Aliakbari, "Numerical study of mixed convection flow in a lid-driven cavity with sinu-

TABLE VII. Mean heat transfer rate variations with different values of Eckert number

Pertinent Parameter	γ-$Al_2O_3 - H_2O$	γ-$Al_2O_3 - C_2H_6O_2$
$Ec = 0.0$	1.665810502131878	9.169208334148351
$Ec = 0.3$	1.665814975702705	9.169209316562142
$Ec = 1.0$	1.665825414042485	9.169211608866878

NOMENCLATURE

U_0	Reference velocity $[ms^{-1}]$
L	Length of the enclosure $[m]$
u, v	Velocity components in x, y directions $[ms^{-1}]$
x, y	Cartesian coordinates $[m]$
T	Temperature of fluid $[K]$
t^*	Dimensional time $[s]$
p	Pressure $[Pa]$
C_p	Specific heat of fluid $[J\,kg^{-1}K^{-1}]$
k	Fluid thermal conductivity $[W\,m^{-1}\,K^{-1}]$
g	Acceleration due to gravity $[m\,s^{-2}]$
K	Permeability of the porous medium $[m^2]$
B_0	Strength of the inclined magnetic field $[kg\,s^{-2}\,A^{-1}]$
Q_0	Dimensional heat source or sink $[W\,m^{-3}]$
X, Y	Non-dimensional distance along x and y co-ordinates
U	Non-dimensional velocity component along X direction
V	Non-dimensional velocity component along Y direction
t	Dimensionless time
P	Dimensionless pressure
Q	Heat generation/absorption coefficient
Pr	Prandtl number
Re	Reynolds number
Da	Darcy number
Gr	Grashof number
Ri	Richardson number
Ha	Hartmann number
Ec	Eckert number
Nu	Nusselt number

Greek symbols

α	Thermal diffusivity $[m^2s^{-1}]$
μ	Dynamic viscosity $[kg\,m^{-1}\,s^{-1}]$
ρ	Density of fluid $[kg/m^3]$
ν	Kinematic viscosity $[m^2/s]$
σ	Electrical conductivity $[S\,m^{-1}]$
β	Thermal expansion coefficient $[K^{-1}]$
Θ	Inclination angle of the magnetic field $[rad]$
Φ	Solid volume fraction
θ	Non-dimensional temperature

Subscripts

p	particle
f	fluid
nf	nanofluid
c	cold surface
h	hot surface
avg	average

soidal heating on sidewalls using nanofluid," Superlattices and Microstructures **51**, 893–911 (2012).

[20] I. Ataei-Dadavi, M. Chakkingal, S. Kenjeres, C. R. Kleijn, and M. J. Tummers, "Experiments on mixed convection in a vented differentially side-heated cavity filled with a coarse porous medium," International Journal of Heat and Mass Transfer **149**, 119238 (2020).

[21] M. S. Ishak, A. I. Alsabery, I. Hashim, and A. J. Chamkha, "Entropy production and mixed convection within trapezoidal cavity having nanofluids and localised solid cylinder," Scientific Reports **11**, 14700 (2021).

[22] H. Shahid, I. Yaqoob, W. A. Khan, and A. Rafique, "Mixed convection in an isosceles right triangular lid driven cavity using multi relaxation time lattice boltzmann method," International Communications in Heat and Mass Transfer **128**, 105552 (2021).

[23] S. Hussain, K. Mehmood, M. Sagheer, and A. Farooq, "Entropy generation analysis of mixed convective flow in an inclined channel with cavity with al2o3-water nanofluid in porous medium," International Communications in Heat and Mass Transfer **89**, 198–210 (2017).

[24] M. Siavashi, V. Bordbar, and P. Rahnama, "Heat transfer and entropy generation study of non-darcy double-diffusive natural convection in inclined porous enclosures with different source configurations," Applied Thermal Engineering **110**, 1462–1475 (2017).

[25] M. Sankar, B. Kim, J. Lopez, and Y. Do, "Thermosolutal convection from a discrete heat and solute source in a vertical porous annulus," International Journal of Heat and Mass Transfer **55**, 4116–4128 (2012).

[26] T. Javed, Z. Mehmood, M. A. Siddiqui, and I. Pop, "Study of heat transfer in water-cu nanofluid saturated porous medium through two entrapped trapezoidal cavities under the influence of magnetic field," Journal of Molecular Liquids **240**, 402–411 (2017).

[27] M. Durairaj, S. Ramachandran, Mehdi, and R. Mohammad, "Heat generating/absorbing and chemically reacting casson fluid flow over a vertical cone and flat plate saturated with non-darcy porous medium," International Journal of Numerical Methods for Heat & Fluid Flow **27**, 156–173 (2017).

[28] B. H. Khan, V. R. Prasad, and R. B. Vijaya, "Thermal radiation on mixed convective flow in a porous cavity: Numerical simulation," Nonlinear Engineering **7**, 253–261 (2018).

[29] K. Raju, P. Prasad, M. Raju, and S. Ramachandran, "Numerical investigation on mhd marangoni convective flow of nanofluid through a porous medium with heat and mass transfer characteristics," International Journal of Engineering and Technology **7**, 256–260 (2018).

[30] M. Sankar, M. Venkatachalappa, and I. Shivakumara, "Effect of magnetic field on natural convection in a vertical cylindrical annulus," International Journal of Engineering Science **44**, 1556–1570 (2006).

[31] E.Reddy and S. Panda, "Mhd natural convection nanofluid flows in a wavy trapezoidal porous enclosure with differentially heated side walls," Journal of the National Science Foundation of Sri Lanka **48**, 57–68 (2020).

[32] Javaherdeh, Korosh, Moslemi, Mehdi, Shahbazi, and Mona, "Natural convection of nanofluid in a wavy cavity in the presence of magnetic field on variable heat surface temperature," Journal of Mechanical Science and Technology **31**, 1937–1945 (2017).

[33] A. H. Pordanjani, S. Aghakhani, A. A. Alnaqi, and M. Afrand, "Effect of alumina nano-powder on the convection and the entropy generation of water inside an inclined square cavity subjected to a magnetic field: Uniform and non-uniform temperature boundary conditions," International Journal of Mechanical Sciences **152**, 99–117 (2019).

[34] Mansour, Armaghani, Chamkha, and Rashad, "Entropy generation and nanofluid mixed convection in a c-shaped cavity with heat corner and inclined magnetic field," The European Physical Journal Special Topics **228**, 2619–2645 (2019).

[35] C. Revnic, T. Groşan, M. Sheremet, and I. Pop, "Numerical simulation of mhd natural convection flow in a wavy cavity filled by a hybrid cu-al2o3-

water nanofluid with discrete heating," Applied Mathematics and Mechanics **41**, 1345–1358 (2020).

[36]K. Al-Farhany, M. F. Al-dawody, D. A. Hamzah, W. Al-Kouz, and Z. Said, "Numerical investigation of natural convection on al2o3–water porous enclosure partially heated with two fins attached to its hot wall: under the mhd effects," Applied Nanoscience (2021).

[37]A. Mahmoudi, I. Mejri, M. A. Abbassi, and A. Omri, "Analysis of mhd natural convection in a nanofluid-filled open cavity with non uniform boundary condition in the presence of uniform heat generation/absorption," Powder Technology **269**, 275–289 (2015).

[38]A. J. Benazir, R. Sivaraj, and O. D. Makinde, "Unsteady magnetohydrodynamic casson fluid flow over a vertical cone and flat plate with non-uniform heat source/sink," International Journal of Engineering Research in Africa **21**, 69–83 (2015).

[39]A. M. Rashad, A. J. Chamkha, M. A.Ismael, and T.Salah, "Magnetohydrodynamics natural convection in a triangular cavity filled with a cu-al2o3/water hybrid nanofluid with localized heating from below and internal heat generation," ASME. J. Heat Transfer **140**, 072502 (2018).

[40]A. M. Rashad, M. A. Mansour, T. Armaghani, and A. J.Chamkha, "Mhd mixed convection and entropy generation of nanofluid in a lid-driven u-shaped cavity with internal heat and partial slip," Physics of Fluids **31**, 042006 (2019).

[41]M. Massoudi and M. B. Hamida, "Mhd natural convection and thermal radiation of diamond–water nanofluid around rotating elliptical baffle inside inclined trapezoidal cavity," Eur. Phys. J. Plus **135** (2020).

[42]S. S. Shah, R. ul Haq, L. B. McCash, H. M. Bahaidarah, and T. Aziz, "Numerical simulation of lid driven flow in a curved corrugated porous cavity filled with cuo-water in the presence of heat generation/absorption," Alexandria Engineering Journal **61**, 2749–2767 (2022).

[43]M. Rahman, H. Öztop, N. Abd Rahim, S. Rahman, and K. Al-Salem, "Mhd mixed convection with joule heating effect in a lid-driven cavity with a heated semi-circular source using the finite element technique," Numerical Heat Transfer Part a-Applications **60**, 543–560 (2011).

[44]O. Ghaffarpasand, "Numerical study of mhd natural convection inside a sinusoidally heated lid-driven cavity filled with fe3o4-water nanofluid in the presence of joule heating," Applied Mathematical Modelling **40**, 9165–9182 (2016).

[45]K. Mehmood, S. Hussain, and M. Sagheer, "Mixed convection in alumina-water nanofluid filled lid-driven square cavity with an isothermally heated square blockage inside with magnetic field effect: Introduction," International Journal of Heat and Mass Transfer **109**, 397–409 (2017).

[46]I. Zahan, R. Nasrin, and M. A. Alim, "Mixed convective hybrid nanofluid flow in lid-driven undulated cavity: effect of mhd and joule heating," Journal of Naval Architecture and Marine Engineering **16**, 109–126 (2019).

[47]M. Taghikhani, "Cu–water nanofluid mhd mixed convection in a lid-driven cavity with two sinusoidal heat sources considering joule heating effect," Int J Thermophys **40** (2019).

[48]A. Alhashash, H. Saleh, and I. Hashim, "Natural convection and viscous dissipation in a square porous enclosure using a thermal nonequilibrium model," AIP Conference Proceedings **1602**, 151–156 (2014).

[49]M. Ghalambaz, M. Sabour, and I. Pop, "Free convection in a square cavity filled by a porous medium saturated by a nanofluid: Viscous dissipation and radiation effects," Engineering Science and Technology, an International Journal **19**, 1244–1253 (2016).

[50]I.Pop and M. Sheremet, "Free convection in a square cavity filled with a casson fluid under the effects of thermal radiation and viscous dissipation," International Journal of Numerical Methods for Heat & Fluid Flow **27**, 2318–2332 (2017).

[51]C.Haritha, C. Balla, and N. Kishan, "Mhd natural convection heat transfer in a porous square cavity filled by nanofluids with viscous dissipation," Journal of Nanofluids **7**, 928–938 (2018).

[52]O. A. Bég, K. Venkatadri, V. R. Prasad, T. Bég, A. Kadir, and H. J. Leonard, "Numerical simulation of hydromagnetic marangoni convection flow in a darcian porous semiconductor melt enclosure with buoyancy and heat generation effects," Materials Science and Engineering: B **261**, 114722 (2020).

[53]R. R. Souza, I. M. Gonçalves, R. O. Rodrigues, G. Minas, J. Miranda, A. L. Moreira, R. Lima, G. Coutinho, J. Pereira, and A. S. Moita, "Recent advances on the thermal properties and applications of nanofluids: From nanomedicine to renewable energies," Applied Thermal Engineering **201**, 117725 (2022).

[54]S. A. M. Mehryan, E. Izadpanahi, M. Ghalambaz, and A. J.Chamkha, "Mixed convection flow caused by an oscillating cylinder in a square cavity filled with cu–al2o3/water hybrid nanofluid," Journal of Thermal Analysis and Calorimetry **137**, 965–982 (2019).

[55]M.Ghalambaz, S. A. M. Mehryan, E. Izadpanahi, A. J. Chamkha, and D. Wen, "Mhd natural convection of cu–al2o3 water hybrid nanofluids in a cavity equally divided into two parts by a vertical flexible partition membrane," Journal of Thermal Analysis and Calorimetry **138**, 1723–1743 (2019).

[56]M. I. Khan, F. Shah, M. Waqas, T. Hayat, and A. Alsaedi, "The role of γ-al2o3-h2o and γ-al2o3-c2h6o2 nanomaterials in darcy-forchheimer stagnation point flow: An analysis using entropy optimization," International Journal of Thermal Sciences **140**, 20–27 (2019).

[57]U. Farooq, H. Waqas, T. Muhammad, M. Imran, and A. S. Alshomrani, "Computation of nonlinear thermal radiation in magnetized nanofluid flow with entropy generation," Applied Mathematics and Computation **423**, 126900 (2022).

[58]T. Islam, M. Alam, and M. Asjad, "Heatline visualization of mhd natural convection heat transfer of nanofluid in a prismatic enclosure," Sci Rep **11** (2021).

[59]M. Uddin and M. Rahman, "Numerical computation of natural convective heat transport within nanofluids filled semi-circular shaped enclosure using nonhomogeneous dynamic model," Thermal Science and Engineering Progress **1**, 25–38 (2017).

Figure A

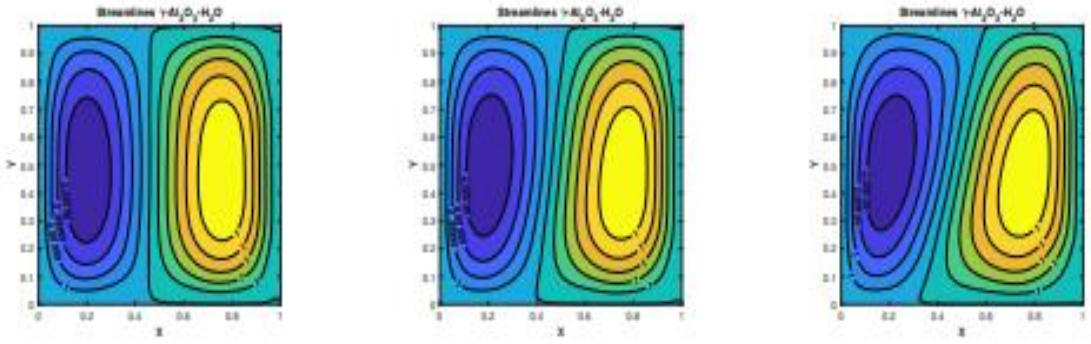

Figure B

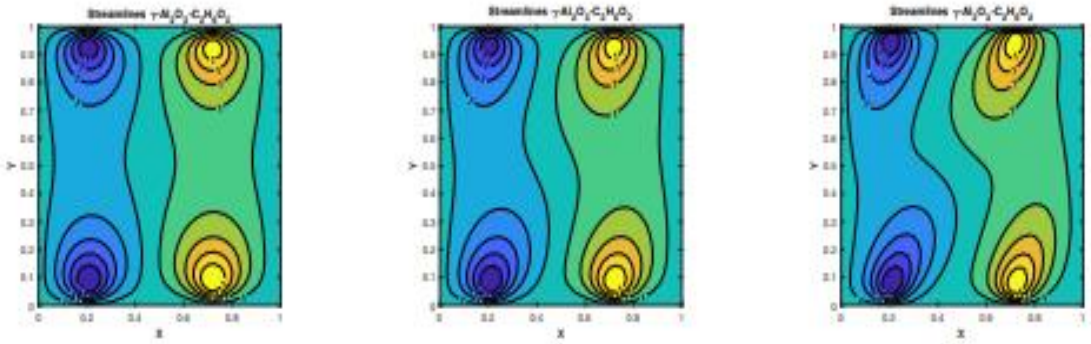

FIG. 3. Streamlines of $(A)\gamma - Al_2O_3 - H_2O$ and $(B)\gamma - Al_2O_3 - C_2H_6O_2$ for different values of (I) $Ha = 10$, (II) $Ha = 50$, (III) $Ha = 100$.

Figure A

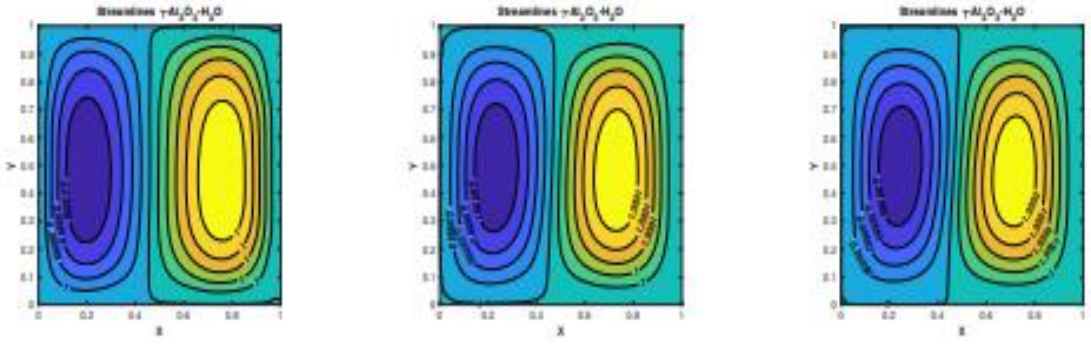

Figure B

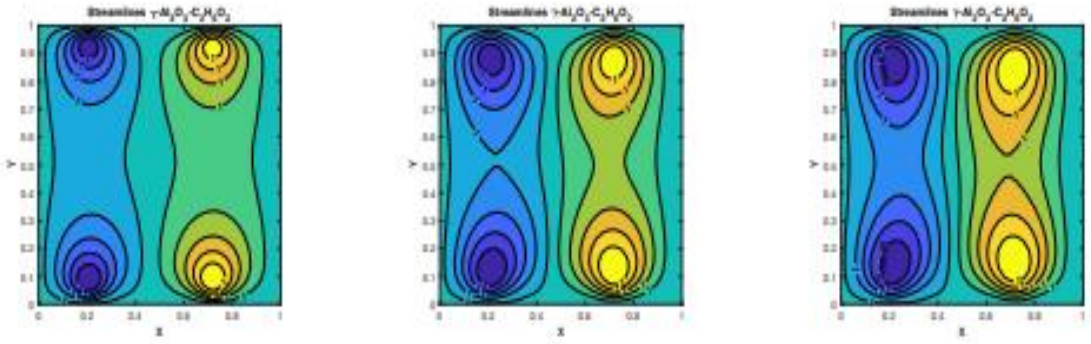

FIG. 4. Streamlines of $(A)\gamma - Al_2O_3 - H_2O$ and $(B)\gamma - Al_2O_3 - C_2H_6O_2$ for different values of (I) $Da = 10^{-3}$, (II) $Da = 10^{-2}$, (III) $Da = 10^{-1}$.

Figure A

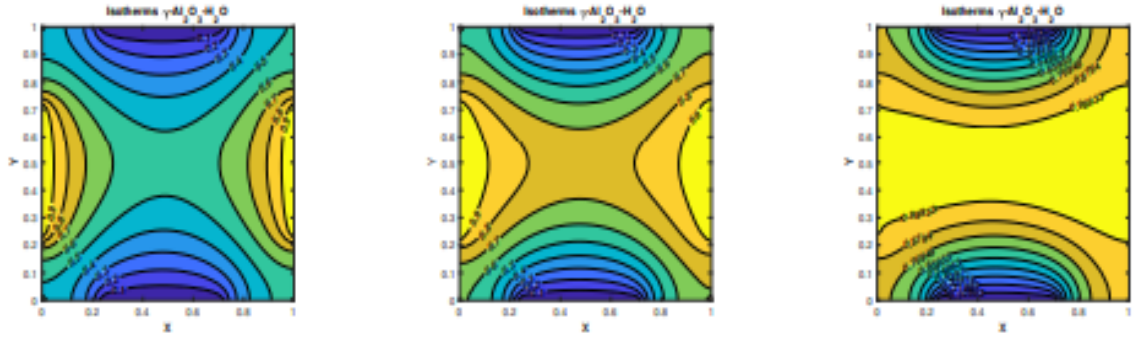

Figure B

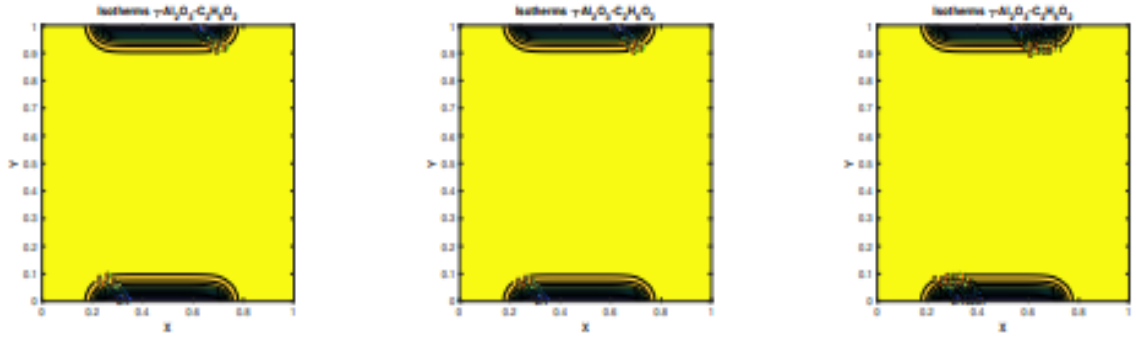

FIG. 5. Isotherms of $(A)\gamma-Al_2O_3-H_2O$ and $(B)\gamma-Al_2O_3-C_2H_6O_2$ for different values of $(I)\ Q=-6$, $(II)\ Q=0$, $(III)\ Q=6$.

Figure A

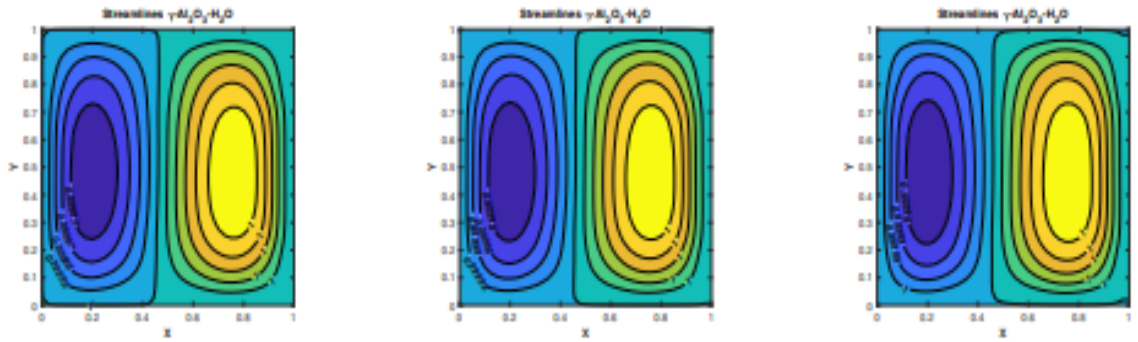

Figure B

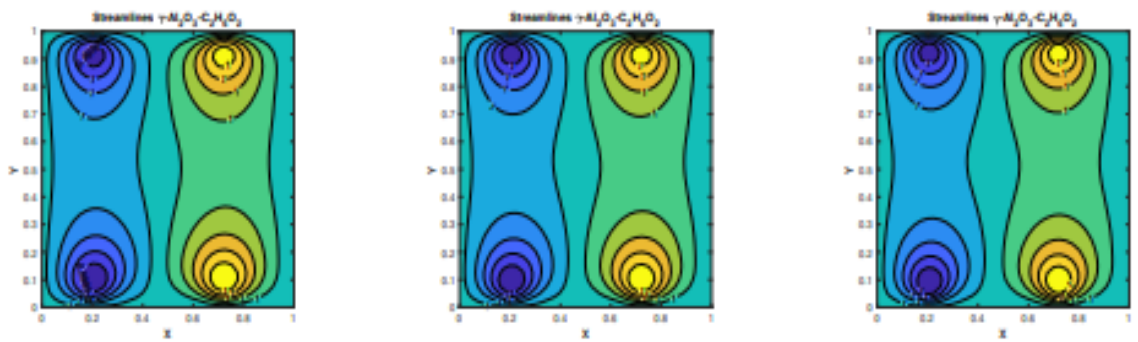

FIG. 6. Streamlines of $(A)\gamma-Al_2O_3-H_2O$ and $(B)\gamma-Al_2O_3-C_2H_6O_2$ for different values of $(I)\ \Phi=0\%$, $(II)\ \Phi=3\%$, $(III)\ \Phi=5\%$.

Figure A

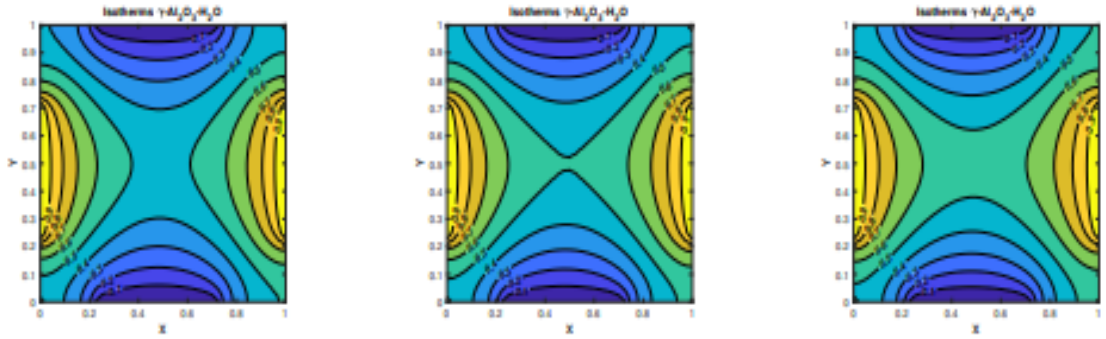

Figure B

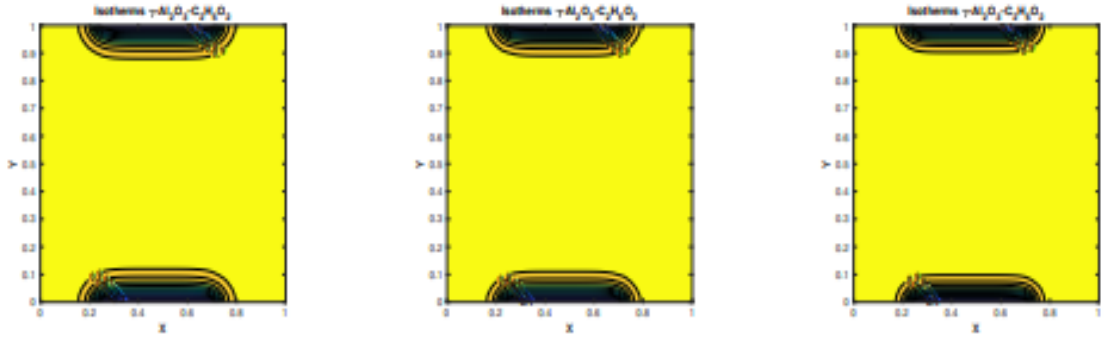

FIG. 7. Isotherms of $(A)\gamma-Al_2O_3-H_2O$ and $(B)\gamma-Al_2O_3-C_2H_6O_2$ for different values of $(I)\ \Phi=0\%$, $(II)\ \Phi=3\%$, $(III)\ \Phi=5\%$.

Figure A

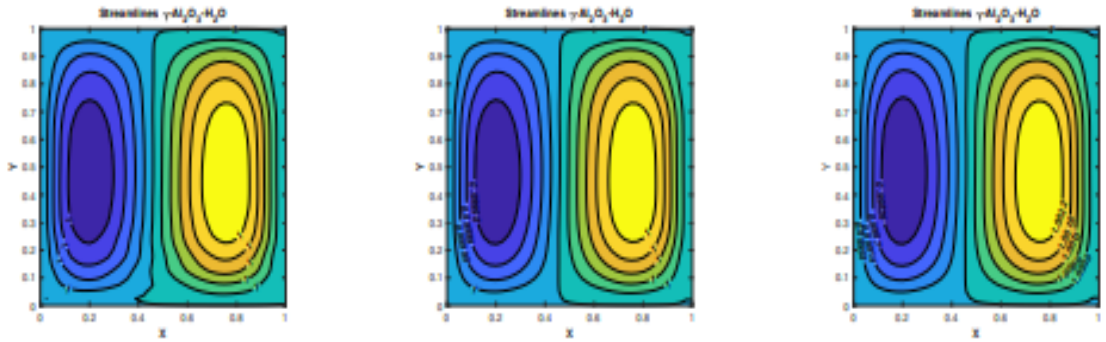

Figure B

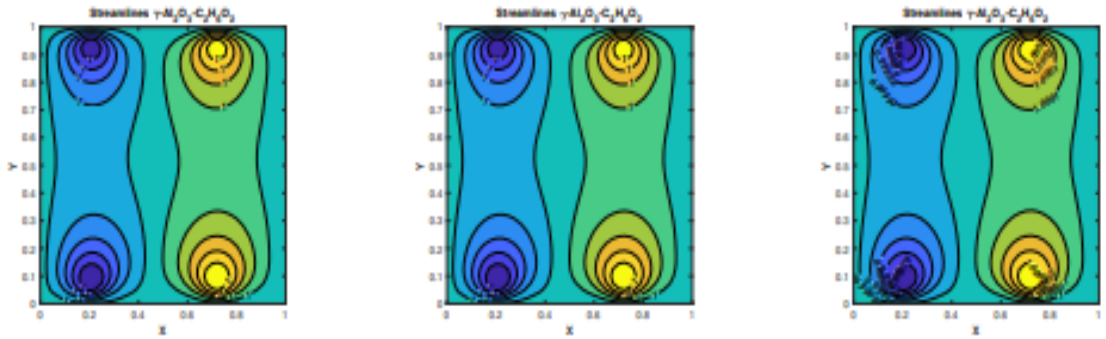

FIG. 8. Streamlines of $(A)\gamma-Al_2O_3-H_2O$ and $(B)\gamma-Al_2O_3-C_2H_6O_2$ for different values of $(I)\ Ri=0.01$, $(II)\ Ri=1$, $(III)\ Ri=100$.

Figure A

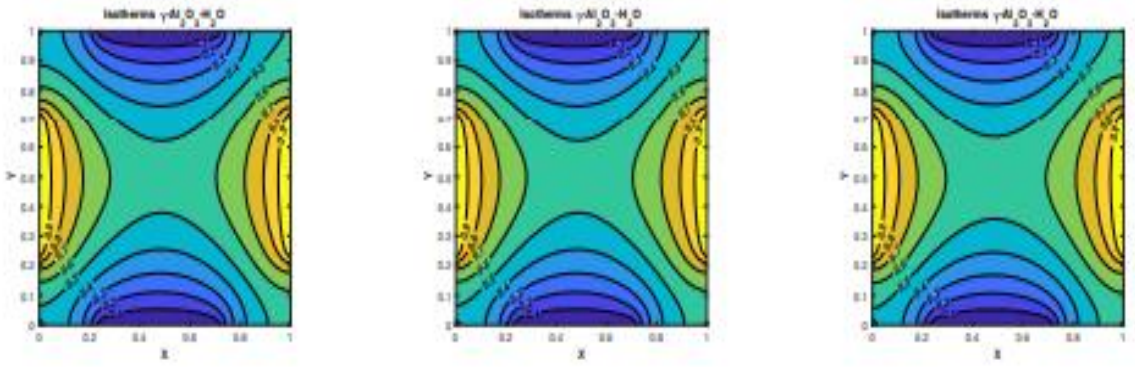

Figure B

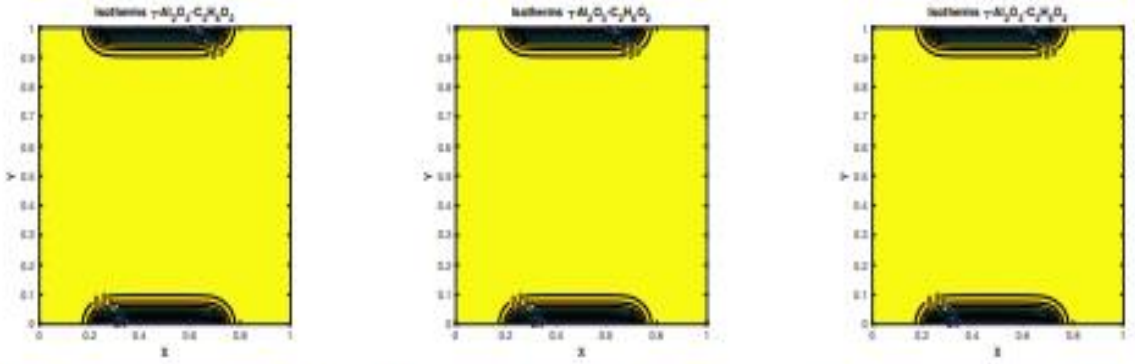

FIG. 9. Isotherms of $(A)\gamma - Al_2O_3 - H_2O$ and $(B)\gamma - Al_2O_3 - C_2H_6O_2$ for different values of (I) $Ri = 0.01$, (II) $Ri = 1$, (III) $Ri = 100$.

Figure A

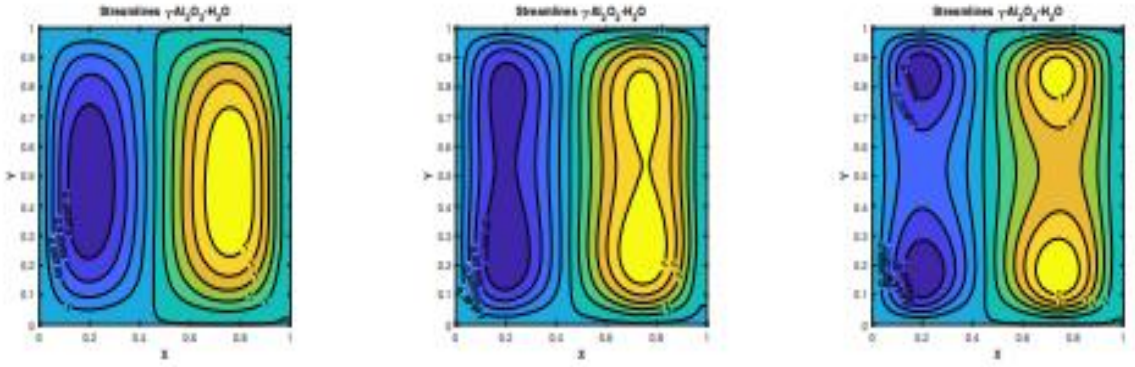

Figure B

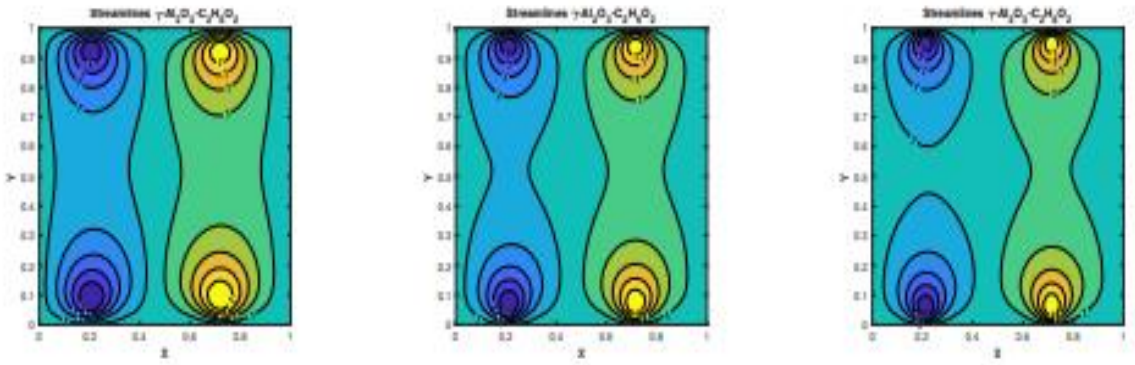

FIG. 10. Streamlines of $(A)\gamma - Al_2O_3 - H_2O$ and $(B)\gamma - Al_2O_3 - C_2H_6O_2$ for different values of (I) $Re = 2$, (II) $Re = 5$, (III) $Re = 10$.

Figure A

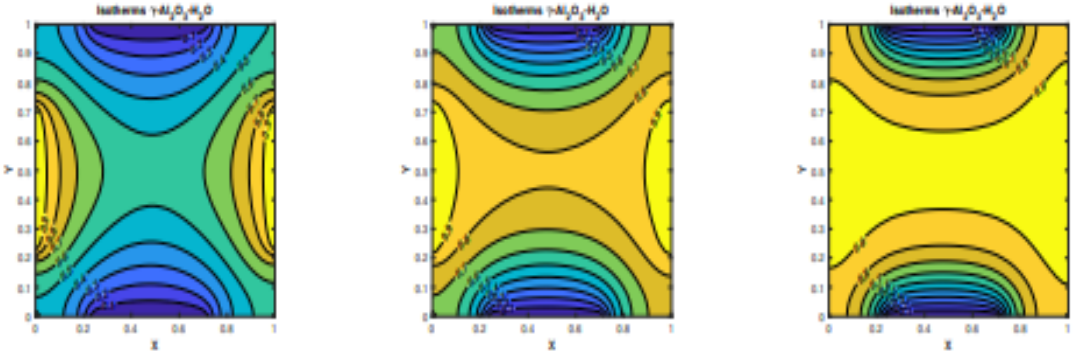

Figure B

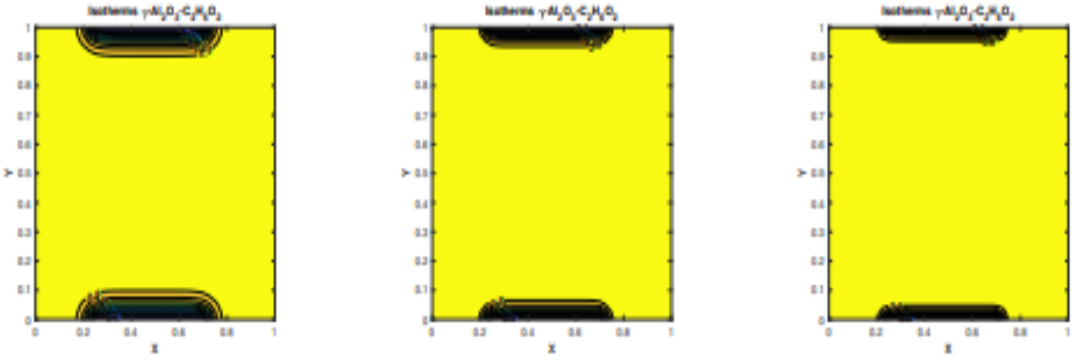

FIG. 11. Isotherms of $(A)\gamma - Al_2O_3 - H_2O$ and $(B)\gamma - Al_2O_3 - C_2H_6O_2$ for different values of (I) $Re = 2$, (II) $Re = 5$, (III) $Re = 10$.

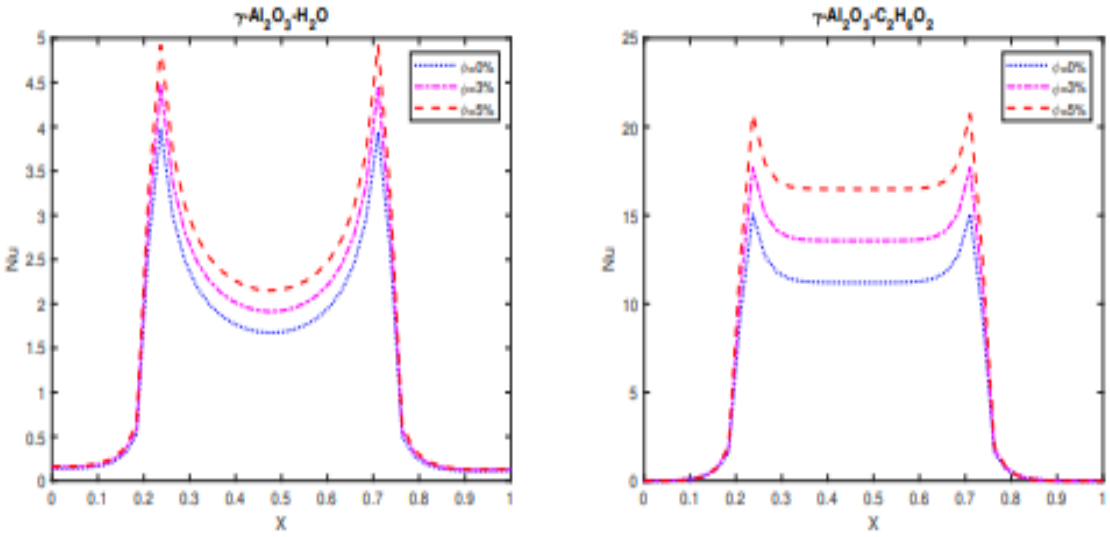

FIG. 12. Local Nusselt number of $(A)\gamma - Al_2O_3 - H_2O$ and $(B)\gamma - Al_2O_3 - C_2H_6O_2$.

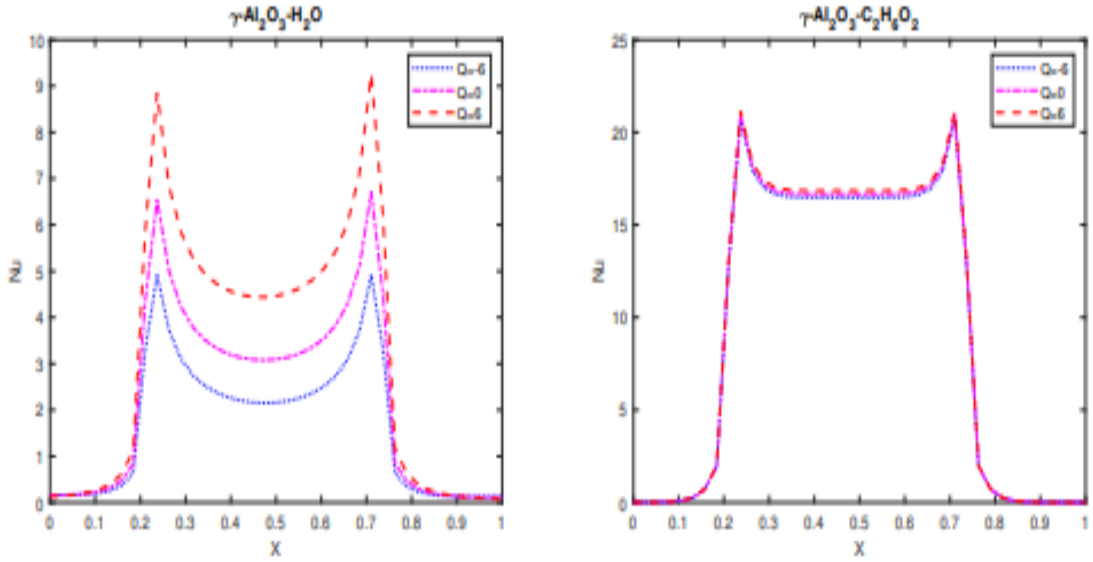

FIG. 13. Local Nusselt number of $(A)\gamma - Al_2O_3 - H_2O$ and $(B)\gamma - Al_2O_3 - C_2H_6O_2$.

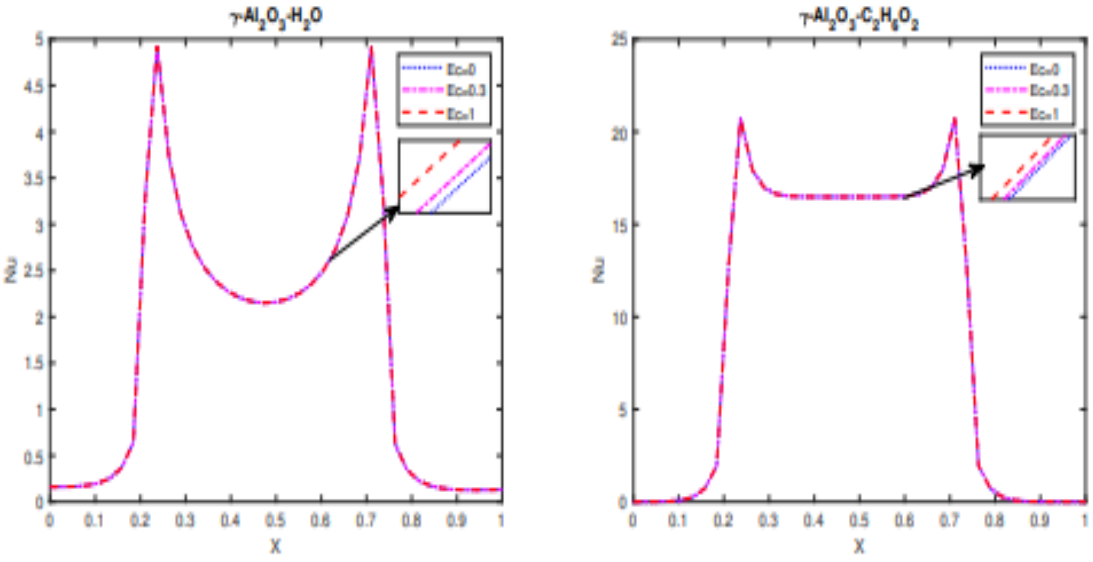

FIG. 14. Local Nusselt number of $(A)\gamma - Al_2O_3 - H_2O$ and $(B)\gamma - Al_2O_3 - C_2H_6O_2$.